NOTE TO USERS

This reproduction is the best copy available.

UMI®

PRELIMINARY DEVELOPMENT OF MEMS-BASED CORROSION SENSOR

PRELIMINARY DEVELOPMENT OF MEMS-BASED CORROSION SENSOR

**A thesis submitted in partial fulfillment
of the requirement for the degree
Master of Science in Mechanical Engineering**

By

**Feng Pan
Shandong University
Bachelor of Engineering in Mechanical Engineering, 2005**

**May 2010
University of Arkansas**

UMI Number: 1484647

All rights reserved

INFORMATION TO ALL USERS
The quality of this reproduction is dependent upon the quality of the copy submitted.

In the unlikely event that the author did not send a complete manuscript
and there are missing pages, these will be noted. Also, if material had to be removed,
a note will indicate the deletion.

UMI 1484647
Copyright 2010 by ProQuest LLC.
All rights reserved. This edition of the work is protected against
unauthorized copying under Title 17, United States Code.

ProQuest LLC
789 East Eisenhower Parkway
P.O. Box 1346
Ann Arbor, MI 48106-1346

ABSTRACT

A MEMS-based solid state corrosion sensor based on the metal particle polymer composite materials has recently been proposed by the Engineered Micro/Nano-Systems Laboratory at the University of Arkansas. The sensor consists of micro/nano-scale metal particles embedded in a polymer (elastomer) matrix. The variability in the chemical and dimensional properties of the sensor element will provide the tailorability in sensor sensitivity, selectivity, time response, and operating life-span. This thesis focuses on the electrical resistivity property of the sensor element and the MEMS-based patterning technique for the fabrication of the sensor element. The investigation of the electrical resistivity as a function of particle mass or volume percentage provides the understanding of the role size plays in the selection of the metal particles.. Three types of particles, carbon, silver-coated aluminum, and nickel, have been studied with the mass percentage ranges of 13-15%, 63-65%, and 64-68%, respectively. Due to the natural oxidation of the metal particle surfaces, a wet etch approach is used to demonstrate the feasibility of oxide removal for particles prior to embedding in the polymer (using HCl on Nickel particles). After etching, these particles are then rinsed by IPA (Isopropyl alcohol), and mixed with polymer material in nitrogen gas environment to prevent further oxidization. The mixed metal particle polymer composite material can then be used to pattern the sensor element. The basic Direct Polymer Patterning On Substrate Technique (DPPOST) is used to microfabricate the sensor element. DPPOST has the ability to form a wide range of structural features found in MEMS, from tens of millimeter structures to micrometer level resolutions. A modified process has been researched to provide higher robustness in

the fabrication process, with the goal of achieving near 100% patterning yields. The modified-DPPOST process uses conformal coating of Omnicoat™ nano-films to provide a barrier between the SU-8® and the patterned polymer, hence reducing stiction during the release process. Research performed in this thesis provides a stepping stone to the further development of a MEMS-based corrosion sensor.

This thesis is approved for
Recommendation to the
Graduate Council

Thesis Director:

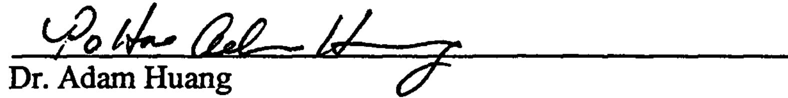
Dr. Adam Huang

Thesis Committee:

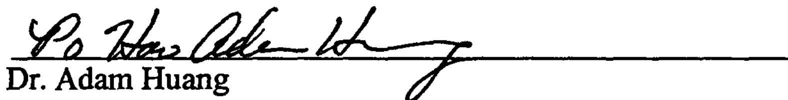
Dr. Adam Huang

Dr. Steve Tung

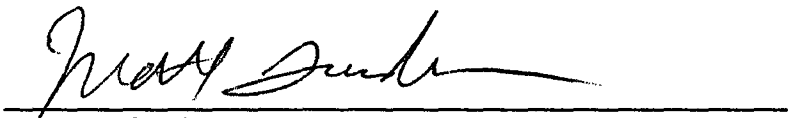
Dr. Matt Gordon

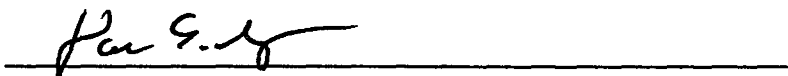
Dr. Douglas Spearot

This thesis is approved for
Recommendation to the
Graduate Council

Thesis Director:

____
Dr. Adam Huang

Thesis Committee:

____
Dr. Adam Huang

____
Dr. Steve Tung

____
Dr. Matt Gordon

____
Dr. Douglas Spearot

THESIS DUPLICATION RELEASE

I hereby authorize the University of Arkansas Libraries to duplicate this Thesis when needed for research and/or scholarship.

Agreed ______________________________
Feng Pan

Refused ______________________________
Feng Pan

ACKNOWLEDGEMENTS

I would like to thank my advisor Dr. Adam Huang for his support, advice and guidance throughout this work. I would also like to thank Drs. Steve Tung, Matt Gordon and Douglas Spearot for serving on my thesis committee.

I would like to thank my research group mates John Lee, Mark Center, Arun Madyala, Matthew McMullen, and Cody Baxter for their beneficial discussion with me.

Last but not least, I would like to thank National Science Foundation (NSF) CMMI-0800718 (Sensor and Sensing Systems SSS-Dr. Shih C. Liu) for its partial financial support to this project in addition to the University of Arkansas start-up fund provided through my advisor.

TABLE OF CONTENTS

ABSTRACT IX

ACKNOWLEDGEMENTS vi

TABLE OF CONTENTS vii

CHAPTER 1 1

INTRODUCTION 1

1.1 Corrosion and Corrosive Monitoring 1

1.2 Objectives 9

1.3 Mechanism of Corrosion Sensor 11

1.4 Electrical Properties of the Sensing Composites 11

1.5 Oxide removal of metal particles 12

1.6 MEMS Fabrication of Sensor Element 13

1.7 Organization of the thesis 14

CHAPTER 2 15

ELECTROCHEMICAL TRANSDUCTION MECHANISM OF METAL PARTICLE POLYMER COMPOSITES 15

2.1 Introduction 15

2.2 Experiment and Data Analysis 18

2.3 Resistivity Measurement 23

CHAPTER 3 29

REMOVAL OF OXIDE ON METAL PARTICLES FOR FABRICATING MEMS-BASED CORROSION SENSOR 29

3.1 Introduction 29

3.2 Experiment 29

3.3 Results and Analysis 33

CHAPTER 4 34

DIRECT POLYMER PATTERNING ON SUBSTRATE TECHNIQUE AND ITS MODIFIED APPROACH 34

4.1 Introduction 34

4.2 DPPOST Fabrication 36

4.3 Modified Approach of the DPPOST 40

4.4 Oxygen Plasma Etching Rate Test 42

4.5 Optimize the Modified DPPOST Technique 45

CHAPTER 5 49

CONCLUSIONS AND FUTURE WORK 49

5.1 Conclusions 49

5.2 Future Work 50

REFERENCES 52

LIST OF FIGURES

FIGURE 1 FLOW CHART OF THE SUB-COMPONENTS TOWARD THE DEVELOPMENT OF THE MEMS-BASED CORROSION SENSOR 10

FIGURE 2 THE PROCESS FLOW OF DPPOST 14

FIGURE 3 THE CORROSION MECHANISM OF THE SENSOR 15

FIGURE 4 THE FIRST STEP CURING TIME VERSUS TEMPERATURE 18

FIGURE 5 SAMPLE WITH CARBON BLACK PARTICLES (LEFT) SAMPLE WITH SILVER-COATED ALUMINUM PARTICLES (RIGHT) 19

FIGURE 6 FORCES ON THE PARTICLE IN THE PDMS SOLUTION PRIOR TO CURING 19

FIGURE 7 SEDIMENTATION TIME VERSUS DISPLACEMENT 21

FIGURE 8 THE TWO-STEP CURING TIME VERSUS TEMPERATURE 22

FIGURE 9 SEDIMENTATION TIME VERSUS DISPLACEMENT WITH RESPECT TO VISCOSITY 22

FIGURE 10 SEDIMENTATION TIME VERSUS DISPLACEMENT 23

FIGURE 11 RESISTIVITY VERSUS MASS PERCENTAGE OF CARBON BLACK PARTICLE 25

FIGURE 12 RESISTIVITY VERSUS VOLUME PERCENTAGE OF CARBON BLACK PARTICLE 25

FIGURE 13 RESISTIVITY VERSUS MASS PERCENTAGE OF SILVER-COATED ALUMINUM PARTICLE 26

FIGURE 14 RESISTIVITY VERSUS VOLUME PERCENTAGE OF SILVER-COATED ALUMINUM PARTICLE 26

FIGURE 15 RESISTIVITY VERSUS MASS PERCENTAGE OF NICKEL PARTICLE SAMPLE 27

FIGURE 16 RESISTIVITY VERSUS VOLUME PERCENTAGE OF NICKEL PARTICLE SAMPLE 27

FIGURE 17 RESISTIVITY VERSUS MASS PERCENTAGE OF NICKEL PARTICLES WITH OXIDE REMOVAL PROCESS 31

FIGURE 18 RESISTIVITY VERSUS MASS PERCENTAGE OF NICKEL PARTICLES WITHOUT OXIDE REMOVAL PROCESS 32

FIGURE 19 RESISTIVITY VERSUS VOLUME PERCENTAGE OF NICKEL PARTICLES WITHOUT OXIDE REMOVAL PROCESS 33

FIGURE 20 THE PROCESS FLOW OF DPPOST 37

FIGURE 21 EXAMPLE OF LIFT-OFF PROBLEMS AT 40X MAGNIFICATION 39

FIGURE 22 PROCESS FLOW OF MODIFIED METHOD FOR THE DPPOST 40

FIGURE 23 CROSS SECTION OF 25MM WIDTH SU-8 LINES PATTERNED ON SUBSTRATE (UPSIDE DOWN), WITH SPIN-COATED OMNICOAT™. LEFT: IMAGE OF CROSS-SECTION OF SU-8® PATTERNS; THE WIDTH OF PATTERNED LINES IS 25MM. RIGHT: THE MAGNIFIED IMAGE OF THE FRAMED AREA 41

FIGURE 24 PROCESS FLOW OF TESTING OXYGEN PLASMA ETCHING RATE 42

FIGURE 25 AFM IMAGES OF CHIPS ETCHED BY DIFFERENT TIME 43

FIGURE 26 OXYGEN PLASMA ETCHING RATE USING APE 110 GENERAL PURPOSE BARREL PLASMA UNIT 44
FIGURE 27 OXYGEN PLASMA ETCHING RATE USING PLASMA-THERM SLR 45
FIGURE 28 VAPOR PRIMING ILLUSTRATION 46
FIGURE 29 THERMAL VAPOR PRIMING ILLUSTRATION 47
FIGURE 30 THERMAL VAPOR PRIMING THICKNESS VS. TIME 47

CHAPTER 1
INTRODUCTION

1.1 Corrosion and Corrosive Monitoring

Corrosion is defined as the destructive and unintended attack of a metallic material, which is associated with electrochemical reactions and starts at the surface of the metal material [1]. The corrosion process that occurs for metals is normally based on the formation of metal oxides and the subsequent degradation of such oxides that then lead to further oxidization of the metal [1,2,3]. The process that metal atoms lose electrons is regarded as the oxidation part of the reduction-oxidation reaction. The electrons generated from the oxidation of the metal atom are then transferred to a reducing reaction, typically generating negative ions of oxygen. These reactions are often more volatile in aqueous solutions due to the enhanced mobility of these ions over the immersed surfaces. An example of the electrochemical corrosion for metal is given by considering the nickel metal. Nickel atoms become positive charged by the oxidation process, while providing the excess electrons needed for the reduction process of the oxygen molecule. The resulting ionic reaction is the formation of the nickel (nickel (III) oxide) on the surface of the metal. The overall "oxidation" reaction of the nickel to form its oxide is

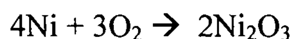

$$4Ni + 3O_2 \rightarrow 2Ni_2O_3$$

The oxidation reaction of nickel atoms is,

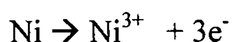

$$Ni \rightarrow Ni^{3+} + 3e^-$$

with the complimentary reduction reaction of

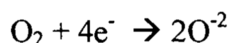

$$O_2 + 4e^- \rightarrow 2O^{-2}$$

Interestingly, in the case of nickel, the formation of the oxide often provides it as a protective barrier. However, this is not the case for most other metals (such as iron,

copper, and brass) where the corrosion of metallic materials causes material loss, stress concentrations, and structural damage. The result is that corrosion leads to considerable cost. The annual cost of corrosion in U.S. is estimated to be about $300 billion (~4% of the gross domestic product) [4,5]. For the petrochemical and pharmaceutical industries alone the annual cost is about $2.5 billion [5]. The large cost to nations suggests that study of corrosion formation and methods of identifying corrosion's forms are crucial.

The damage from corrosion can take many forms. There are several different methods to categorize the types of corrosion. A widely acceptable classification based on three standards is shown below [6]:

1. Those recognizable with the unaided eye.
2. Those that are more easily discerned with specific aids (e.g., dye penetrants, microscopy).
3. Those that can only be identified definitely by optical or electronic microscopy.

According to the above standards, there exist nine types of corrosion forms.

1. Uniform attack

Uniform attack causes the metal to be consumed uniformly over the entire surface that is wetted within the corrosive environment. The penetration of metal by corrosion at any point on the surface is no greater than twice of the average rate. Uniform attack is usually the least threatening type of attack, allowing one to forecast with some accuracy the probable life of equipment. Except in rare cases of a grossly improper choice of material for a particular service, failures of metals by uniform attack are not often encountered.

However, uniform attack is the most common corrosion form in reality, such as the internal corrosion of pipeline, the corrosion of the buried or immerged steel structures, and the corrosion of copper alloy under seawater. From the point view of measurement, uniform attack is detectable and its effect is predictable. Therefore, monitoring uniform attack is less challenging comparing with other types of corrosion (introduced later). Our MEMS-based sensor is designed to monitor the uniform attack.

2. Pitting corrosion

Pitting corrosion is a localized form of corrosion by which cavities or "holes" are produced in the material. Pitting is considered to be more dangerous than uniform corrosion damage because it is more difficult to detect, predict, and design against. A small, narrow pit with insignificant overall material loss can lead to the failure of an entire engineered system.

3. Crevice corrosion

Crevice corrosion occurs in cracks or crevices formed between mating surfaces of metal assemblies, and usually takes the form of pitting or etched patches. Both surfaces may be of the same metal or of dissimilar metals. It can also occur under scale and surface deposits and under loose-fitting washers and gaskets that do not prevent the entry of liquid between them and the metal surface. Crevices may proceed inward from a surface exposed to air, or may exist in an immersed structure.

4. Galvanic corrosion

Galvanic corrosion refers to corrosion damage induced when two dissimilar materials are coupled in a corrosive electrolyte. In metallic couple, the less noble material becomes the anode and tends to corrode at an accelerated rate, compared with the uncoupled condition,

while the more noble material will act as the cathode in the corrosion cell. The electrical connection needed to complete the circuit is provided by the contact between the two metals. The rate of corrosion activity is governed by the relative positions of the metals in the galvanic series, the more widely separated the metals are in the series the faster is the corrosion due to the greater difference in the electrochemical potential between them.

5. Erosion-corrosion

Erosion–corrosion is associated with a flow-induced mechanical removal of the protective surface film that results in a subsequent corrosion rate increase via either electrochemical or chemical processes. It is often accepted that a critical fluid velocity must be exceeded for a given material for this type of corrosion to be severe. The mechanical damage by the impacting fluid imposes disruptive shear stresses or pressure variations on the material surface and/or the protective surface film. The morphology of surfaces affected by erosion–corrosion may be in the form of shallow pits, horseshoe shapes, or other local patterns related to the flow direction [6].

6. Fretting corrosion

Fretting corrosion refers to corrosion damage at the asperities of contacting surfaces. Such damage is induced under load and in the presence of repeated relative surface motion, as induced, for example, by vibration. Pits or grooves and oxidized debris characterize this damage, typically found in machinery, bolted assemblies, and ball or roller bearings [6].

7. Intergranular corrosion

Intergranular corrosion is a form of localized attack in which a narrow path is corroded out preferentially along the grain boundaries of a metal. It initiates on the

surface and proceeds by local cell action in the immediate vicinity of a grain boundary. Although the detailed mechanism of intergranular corrosion varies with the metal system, its physical appearance at the microscopic level is quite similar for most systems. The effects of this form of attack on mechanical properties may be extremely harmful. The driving force is a difference in corrosion potential that develops between a thin grain boundary zone and the bulk of the immediately adjacent grains. The difference in potential may be caused by a difference in chemical composition between these two zones. Such a difference may develop as a result of migration of impurities or alloying elements in an alloy to the grain boundaries. If the concentration of alloying elements in the grain boundary region becomes sufficient, a second phase or constituent may separate or precipitate. This may have a corrosion potential different from that of the grains (or matrix) and cause a local cell to form.

8. Dealloying

Another type of localized corrosion involves the selective removal by corrosion of one of the elements of an alloy by either preferential attack or by complete dissolution of the matrix. Various kinds of selective dissolution have been named after the alloy system that has been affected, usually on the basis of the element dissolved.

9. Environmental cracking

Mechanical forces usually have little if any effect on the overall corrosion of metals. Compressive stresses do not cause cracking. In fact, shot peening is often used to reduce the susceptibility of metallic materials to fatigue, and other forms of cracking. Environmental cracking is defined as the brittle fracture of a normally ductile material in which the corrosive effect of the environment is a factor. Environmental cracking can

occur with a wide variety of metals and alloys and includes all of the types of corrosion failures listed below:

- Corrosion fatigue.
- Hydrogen embrittlement.
- Hydrogen-induced cracking (HIC), a cathodic process.
- Hydrogen stress cracking.
- Liquid metal cracking (LMC), usually a physicochemical process.
- Stress corrosion cracking (SCC), an anodic process.
- Sulfide stress cracking (SSC).

For different types of corrosion, the first step to solving corrosion problems is corrosion monitoring. Corrosion monitoring refers to corrosion measurements performed under industrial or practical operating conditions. In its simplest form, corrosion monitoring may be described as acquiring data on the rate of material degradation. For detecting and controlling the corrosion deterioration, the corrosion monitoring techniques must be developed and is actually considered as a mature field. However, it depends on what one would call maturity when the associated cost is still prohibitively high. In general, there are three types of corrosion monitoring techniques [5]: offline, online, and real-time measurements. The typical offline measurement is based on the application of material coupons that have composition similar to that of the process equipment of interest. The measurement data usually come from measured change of metal thickness (such as from ultrasonic inspection on coupon components or electrical resistance measurement) or weight loss of coupons [30]. It takes months, even years sometimes, to finish measurement and data collection by offline approach [30]. Data collected indicate

corrosion only after the deterioration has occurred. Offline measurement can only provide average corrosion rate in the data collection period and does not provide any information of the peak corrosion rates and its associated conditions.

For online measurement, the probe used to monitor corrosion is connect to a data memory device that is able to record data of corrosion rate measurements automatically over weeks or months. However, the data acquired cannot be accessed or processed in real-time. Another disadvantage is the corrosion information only can be obtained after the damage has happened.

In the above two approaches, problems are viewed after the corrosion damage and cannot directly link causes and effects immediately, thus preventing mitigation efforts. In order to continuously monitor the corrosion and obtain feedback data, real-time measurement techniques is used [30]. The real-time measurement uses on-board memory of a single transmitter to transport corrosion data [5]. It often applies advanced electrical measurement techniques with analysis algorithms such as Harmonic Distortion Analysis (HDA) to provide higher corrosion rate reporting in real-time [5, 6].

Real-time measurement techniques can monitor large process equipment by distributing sensors across the equipment. This often results in using a large amount of sensors for real-time measurement of large structures or infrastructures. Traditionally, a sensor probe is made by using the same or similar metal material to that of the monitored equipment. The sizes of these sensors are often on the order of centimeters and have long sensor time constants (from minutes to hours). For example, T. Prosek and M. Kouril's real time corrosion monitoring device in atmospheric conditions yields a time response of 1-2 hours [7]. A recent report from Russell Kane reported a 7 minutes response time.

However, the performance between sensitivity and life is often coupled (high sensitivity yields a short life sensor due to the design of the sensing element) [8].

Thus, the two key attributes of the proposed Micro-Electro-Mechanical System (MEMS) sensor are high sensitivity and long sensor life, in addition to other possible advantages typical of MEMS devices. MEMS technology has been successful in the physical sensing context and has yielded a range of small, rugged and inexpensive devices such as accelerometers, strain gauges, microphones, air mass flow sensors, pressure sensors, and more recently gyroscopes and yaw-rate sensors [39]. Some MEMS sensors have been developed to meet the demanding needs of the automotive industry and are used by the millions in engine management systems, to trigger air bags and in anti-rollover, vehicle stability control, and GPS navigation systems [39]. It terms of chemical (gas) sensing, the predominant sensing material used in MEMS is based on metal oxide thin films. These are relatively simple chemo-resistive devices while several more complex MEMS-based gas sensors based on techniques such as NDIR (non-dispersive IR absorption), thermal conductivity, and photoacoustics, together with micro-spectrometers, have recently enjoyed a limited but growing degree of commercial success [39]. However, the common problem in such devices is its degraded performance when compared to the benchmarking method of mass-spectroscopy. For example, miniaturized NDIR sensors suffer from low sensitivities due to the necessarily short optical path-lengths involved, restricting their use to applications involving relatively high gas concentrations [39].

MEMS technology has exerted an impact on physical sensing and growing impact on gas sensing, but currently is of minimal impact on chemical sensing. MEMS technology

is able to provide batch processing (low cost), lithographic alignment (high resolution), small device (decrease material weight, power and high sensitivity), and IC compatibility (smartness). For example, a MEMS chemical vapor sensor (with sensor element dimension of 400μmX400μmX25μm with response time on the order of seconds) has been fabricated using the Direct Polymer Patterning On Substrate Technique, [9, 10] from which the MEMS corrosion sensor currently under development as part of this thesis is derived.

1.2 Objectives

This thesis presents the preliminary work of my doctorate research project, which is to develop a MEMS-based corrosion sensor with metal particle polymer composites. It includes three main objectives and their related tasks (my overall research focus being shown in bold):

1. **Design and fabricate the metal particle polymer composite sensor.**

   ***Selection of metal particles (type, size, percentage)**

   ***Choose proper polymer for matrix usage**

   ***Determine sensor dimension and fabrication parameters**

2. **Study the diffusion of gas molecules through the composite material and the associate corrosion properties.**

   ***Experimentally investigate gas diffusion and test the diffusion coefficients**

   *Apply Molecular Dynamics (MD) simulation to study the discrete atomic mechanisms associated with gas molecule diffusion through the polymer membrane

3. Correlate corrosion rate to electrical resistivity of metal particle polymer composites.

***Experimentally measure sensor characteristics by using Electrical Resistance (ER), and Electrochemical Noise (ECN)**

*Develop a coupled diffusion corrosion model to study the passivation of the metallic particles due to gas molecule interactions.

The figure below shows the relational diagram of the objective.

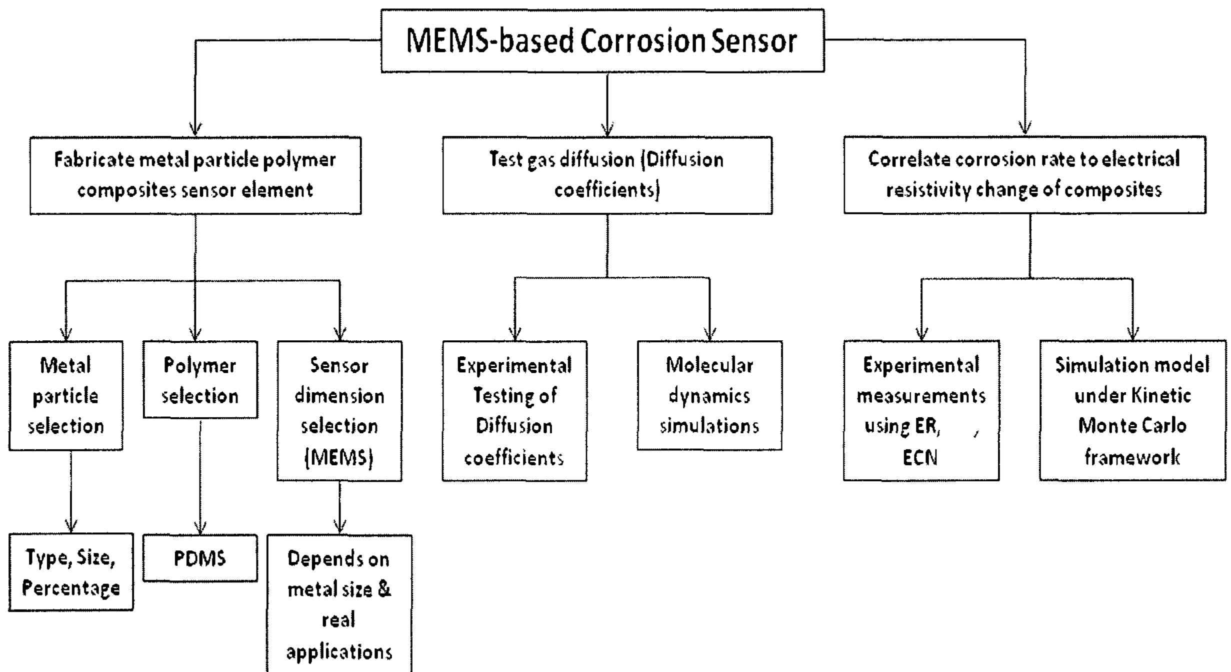

Figure 1 Flow chart of the sub-components toward the development of the MEMS-based Corrosion Sensor

The objectives of this thesis research are to characterize the electrical resistivity property with respect to metal particle mass and volume percentage of three types of metal; to perform preliminary experiment to remove oxides of nickel particles for the future investigation of oxide removal of other types of metal particles; to provide a

modified fabrication technique to achieve better pattern yield in the sensor fabrication. These studies will provide useful data for the further development of the corrosion sensor, which would be my Ph. D dissertation project.

1.3 Mechanism of Corrosion Sensor

The mechanism of the corrosion sensor is based on the mass transport of corrosive species through the sensor matrix [11, 12]. When the metal particles embedded in the matrix corrode, the electrical resistivity increases, due to the increase of particle resistances. The resistivity change can be converted to electrical signal that can be detected to monitor corrosion rate. This type of sensor has high sensitivity due to its micro-size; it also has the ability to tailor the dimension of the composite material thanks to the MEMS-based fabrication technique. As mentioned above, to successfully fabricate the corrosion sensor, the fundamental parameters related to sensor element material (metal particle type, size, and mass percentage in composites), sensor electrical properties (electrical resistivity), and fabrication technique (MEMS-based polymer pattering technique) needed to be determined first, as presented in this thesis.

1.4 Electrical Properties of the Sensing Composites

The first work done in the thesis is to experimentally determine the electrical resistivity of different composites that consist of different metal particles. Because the electrical path is formed by the contact of metal particles between each other in the matrix [9, 10], the conductivity of the composite also depends on the mass percentage of the metal particle (see chapter 2 section 2.1). The characterization of the electrical properties of the material, especially the resistivity, as a function of metal particle mass percentage (which is related to the volume percentage through the material density) is

measured. Three types of particles (carbon, silver-coated aluminum and nickel) are tested. Carbon particle has been tested in previous experiments involving the chemical vapor sensors. Silver-coated aluminum particles are tested because their surfaces are noble and less susceptible to oxidation or other effects so that they can be used as a reference sensor to cancel out undesired but inherent factors such as temperature, humidity, and pressure. Additionally, due to the sedimentation of metal particles in polymer matrix during the mixing of the metal particles and the polymer, the difficulty of homogenous mixture of particles with matrix occurs. To solve the sedimentation problem, a two step cure approach to cure polymer is demonstrated in the description of electrical property characterization.

1.5 Oxide removal of metal particles

It has been discovered during experiments to measure the electrical resistivity of aluminum and stainless-steel that an insulative barrier exists on the particle. Although the extent of this effect depends on the type of metals and metal-oxides, it results in the variability of the resistivity measurements and ultimately will affect sensor sensitivity. For example nickel oxide (NiO or Ni_2O_3), is electrically insulative although not as fast forming as aluminum oxides, resulting in reduced electrical conduction when compared to those of pure nickel particle. Due to the relatively large surface area to volume ratio of micro size particles, the surface insulation effect can dominate the sensor performance in the MEMS corrosion sensor under development.

This thesis provides an oxide removal approach based on the wet etching technique using acidic solutions that reacts specifically with the oxidized coating of different metal particles (etching of nickel oxides using hydrochloric acid was demonstrated). The

resulting solution of the acid and metal particles is then repeatedly diluted and partially-dumped using IPA (Isopropyl alcohol), thus preventing the re-oxidization of the metal. The remaining metal is collected and baked in inert gas (N_2) environment to prevent the further oxidation of the metallic surface so that the collected metal particles can be used in the sensor fabrication. The experiment done as part of this thesis demonstrated the dramatic decrease in the resistivity of the nickel particles after performing oxide removal. But future work is needed to find out the appropriate acids for different type of metal particles such as aluminum or steel. For example, hydro fluoric (HF) acid is proposed to etch aluminum oxide [14]; acetic acid can be used to etch copper oxide without attacking copper [15]. However, emphasis will be made to avoid highly toxic chemicals like HF whenever possible.

1.6 MEMS Fabrication of Sensor Element

The fabrication technique used to pattern the MEMS sensor element is called Direct Polymer Patterning On Substrate Technique (DPPOST), which was developed to pattern polymer (elastomers) based on lift-off technique [3, 13]. As shown in the Fig. 2, the DPPOST is similar to lift-off approach. It employs the Omnicoat™ as the sacrificial layer to remove the supporting wall surrounding the desired pattern. DPPOST has been proved to be a successful technique for fabricating polymer based material that are difficult to etch or deposit. But due to our goal to achieve near 100% fabrication yield, a modified approach to DPPOST is provided in this thesis based on forming a vertical Omnicoat™ layer to reduce the stiction between the polymer and the mold.

Figure 2 The process flow of DPPOST

2.7 Organization of the thesis

This thesis is divided into six chapters. The present chapter gives an introduction and overview of the thesis. In Chapter 2, the electrochemical transduction mechanism of metal particle polymer composites is described. In Chapter 3, the removal of metal oxide of nickel particles by wet etching is presented. In Chapter 4, the fabrication techniques of Direct Polymer Patterning On Substrate Technique (DPPOST) and its modified approach are shown. Finally, Chapter 5 summarizes the conclusions and proposed studies for future work.

CHAPTER 2
ELECTROCHEMICAL TRANSDUCTION MECHANISM OF METAL PARTICLE POLYMER COMPOSITES

2.1 Introduction

In this chapter the electrical properties of metal particle polymer composites is discussed. As mentioned above, the mechanism of the corrosion sensor is based on the mass transport of corrosive species through the sensor matrix. As illustrated in Fig. 3, when the metal particles in the matrix corrode, the electrical resistivity of the material increases due to increasing particle resistances or reduction of conducting surfaces. The MEMS-based fabrication of this sensor design directly results in the ability to control the dimensional properties of the metal particles and polymer matrix, which provides the tailorability in sensor sensitivity, selectivity, time response, and operating life-span.

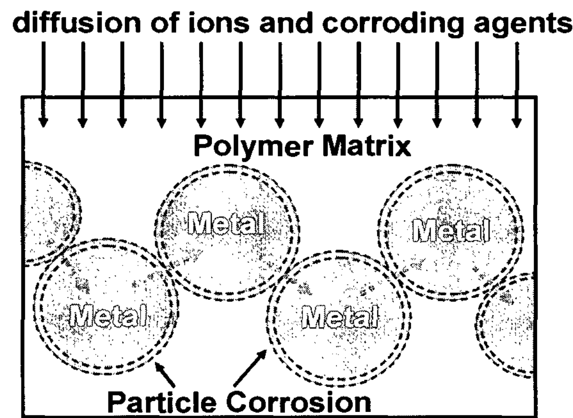

Figure 3 The corrosion mechanism of the sensor

Because the electrical path is formed by the contact of metal particles between each other in the matrix [16, 17], the conductivity of the composite also depends on the mass percentage of the metal particles (or more correctly the volume percentage). For the purpose of engineering the sensor performance, studies of mass and volume percentage of particles in PDMS versus resistivity have been conducted. The sample particles chosen

in the preliminary test are carbon-black, silver-coated aluminum, and nickel particles. Carbon-black and silver-coated aluminum particles are less susceptible to oxidization and corrosion in natural environment. Therefore both can be used as the reference sensor to subtract inherent but undesired sensitivities, such as temperature and pressure. The nickel particles are then used as the target material for corrosion sensing. The particle-composite fabrication procedure encountered complications when the particle material density becomes much larger than the PDMS or when the size of the particle is on the micron-level or larger. The particles will sink to the bottom due to the gravity force acting on it, thereby cause a non-homogenous mixture. To solve this problem, a two step curing approach to treat PDMS has been described in this section.

Another design characteristic of the MEMS corrosion sensor being developed is the inert matrix material in the form of the PDMS polymer. PDMS polymer is a widely used material in MEMS due to their unique properties, including high chemical inertness, electrical insulating, surface properties, proper thermal/electrical insulation and stability, and low Young's modulus [18]. Since the sensor design is itself in micro-scale, the proportion of corrosive material loss of a directly exposed sensing element will be invariably fast, resulting in a reduced sensor life. Thus, the PDMS matrix material for the corrosion sensor will slow down the metal particle corrosion rate, resulting in prolonged sensor life. Furthermore, the large increase in electrical resistivity due to a small increase in particle spatial separation (or due to insulation from oxidation) provides inherent sensor amplification, counterbalancing the reduced sensor sensitivity due to the inert PDMS coating. The sensor sensitivity is also inherently increased due to the relatively large surface area of the sensing element, when compared to the traditional analogs [19].

The electrical resistance (ER) technique is been used here to measure the electrical resistivity as a function of mass (or volume) changes [20]. ER is an "on-line" method of monitoring the rate of corrosion and the extent of total metal loss for any metallic equipment or structure. The ER technique measures the effects of both the electrochemical and the mechanical components of corrosion such as erosion or cavitations. It is the only on-line, instrumented technique applicable to virtually all types of corrosive environments [20]. Although universally applicable, the ER method is uniquely suited to corrosive environments having either poor or non-continuous electrolytes such as vapors, gases, soils, "wet" hydro-carbons, and non-aqueous liquids [20].

Another corrosion measurement is Electrochemical Noise (ECN). It refers to the electrical fluctuations in the corrosion potential and corrosion current flow. ECN monitoring can be further subdivided into electrochemical potential noise (ECPN) measurements and electrochemical current noise (ECCN) measurements [22]. The combined monitoring of potential and current is particularly useful, leading to full electrical impedance measurement. Fluctuations in the corrosion potential can indicate a change in the thermodynamic state of corrosion processes; while changes in the current noise are indicators of the corrosion kinetics [23]. The combination of potential and current noise measurements has also been used to estimate corrosion rates; the methodology is related to measuring the polarization resistance. Electrochemical noise data can provide an indication of the type of corrosion damage that is occurring; it is widely used to distinguish between general and localized attack. The severity of localized can also be gauged by the number and shape of the noise transients [22].

For the measurement of resistivity versus mass (volume) percentage, ER would be applied. ECN would be applied in future measurement due to the more complex instrumentation required that is beyond the scope of this thesis work..

2.2 Experiment and Data Analysis

In the experiments described here, the carbon-black (Carbon black, acetylene, 100% compressed, diameter 45nm, 500g bulk), silver-coated aluminum (-200mesh, Ag 19-21 wt/%, diameter 74μm, 100g bulk), and nickel (-325mesh, diameter 44μm, 500g bulk) particles are purchased from Alfa Aesar®, Inc. The PDMS base and cross-linking agent (Sylgard® 184) are purchased from Dow Corning Company. The mixture ratio used for the PDMS monomer and cross-linker is 10:1. After the PDMS is prepared, it is then mixed with the particle materials. A plastic mold, as shown in Fig. 4, with two gold-plated pins (fixed by epoxy) separated by a channel groove is used for resistivity tests. The composite mixture are then squeegeed into the plastic mold with standard microscope slides, as shown in Fig. 5. The size of the groove is 6.35mm x 2.54mm x 2.032mm (Length x Depth x Width). The sample is cured in a microclimate chamber (CSZ® Inc. MCBH) at temperatures and durations depending on the specific experiment. Two different samples with carbon black composite and silver-coated aluminum composite filled up, respectively, are also shown in Fig. 5.

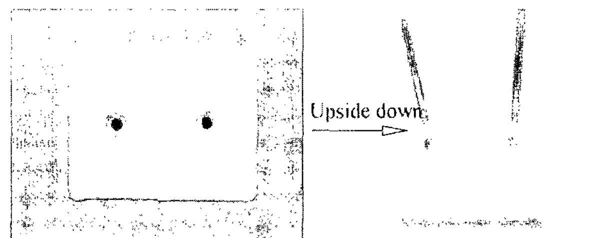

Figure 4 The first step curing time versus temperature

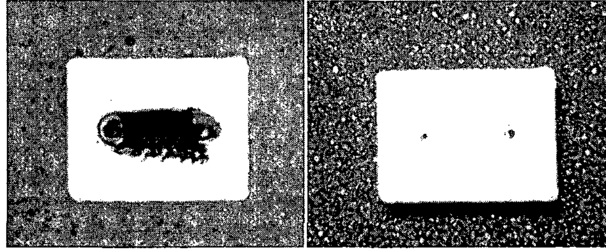

Figure 5 Sample with carbon black particles (Left) Sample with silver-coated aluminum particles (Right)

The particle-composite fabrication procedure above encountered complications when the particle density becomes much larger than the PDMS or when the size of the particle is on the micron-level or larger. Since the particle densities (carbon~2.267g/cm^3, silver-coated aluminum~4.258g/cm^3, and nickel~8.908g/ cm^3) are higher than those of the PDMS (1.03g/cm^3), these particles will settle down at the bottom even after mixing them homogenously, which causes inaccurate resistance measurement. The particle sedimentation time can be calculated by Newton's second law and Stokes' Law. As shown in Fig. 6, the kinematics of the single particle in aqueous PDMS is defined by gravity force, buoyant force, and friction forces.

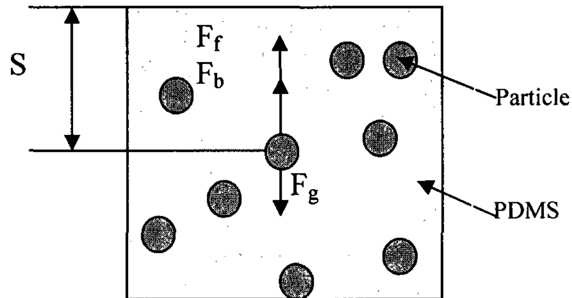

Figure 6 Forces on the particle in the PDMS solution prior to curing

According to Newton's second law, where, F_g, F_b and F_f are gravity force, buoyant force and friction force, respectively. Because,

$$ma = F_g - F_b - F_f \quad (1)$$

$$ma = \rho_{particle} \times V_{particle} \times \frac{d^2 s}{dt^2} \quad (2)$$

$$F_g = \rho_{particle} \times g \times V_{particle} \quad (3)$$

$$F_b = \rho_{PDMS} \times g \times V_{particle} \quad (4)$$

and with Stokes' Law
$$F_f = 6 \times \pi \times \mu_{PDMS} \times R_{particle} \times \frac{ds}{dt} \quad (5)$$

Where, m is the mass of a single particle; a is the acceleration of the particle; g is the gravitational constant; $\rho_{particle}$ is the density of the particle; ρ_{PDMS} is the density of PDMS; $V_{particle}$ is the volume of single particle; μ_{PDMS} is the viscosity of PDMS; and $R_{particle}$ is the radius of the particle. Combine the five equations above, equation (1) can be written as:

$$\rho_{particle} V_{particle} \frac{d^2 s}{dt^2} = \rho_{particle} g V_{particle} - \rho_{PDMS} g V_{particle} - 6\pi\mu_{PDMS} R_{particle} \frac{ds}{dt} \quad (6)$$

Solving this second order ordinary derivative equation, the general solution of the displacement is,

$$\frac{1}{6\pi\mu_{PDMS} R_{particle}} [-C_1 \rho_{particle} V_{particle} e^{-\frac{6\pi\mu_{PDMS} R_{particle}}{\rho_{particle} V_{particle}} t} + g V_{particle} (\rho_{particle} - \rho_{PDMS}) t + 6\pi\mu_{PDMS} R_{particle} C_2] \quad (7)$$

For the case of a static particle starting at the top of the mixture, the initial displacement and velocity are both zero. The boundary condition is listed as S(0)=0; S'(0)=0. According to the initial conditions the constants C1 and C2 can be solved so that particle sedimentation time can be calculated by equation (7). For instance, the silver-coated aluminum, with a nominal diameter 74 μm and density of 4.258g/cm^3 (using density of silver~10.49g/cm^3 and aluminum~2.70g/cm^3 at 20 wt-% Ag) is used to calculate its sedimentation time in PDMS. The viscosity of the PDMS, μ_{PDMS} , is 4.575Pa•s. Using the known parameters and the two boundary conditions, the

sedimentation time versus distance can be plot as shown in Fig. 7. Since the depth of the sample holder is S=2.54mm, from Fig. 7 it indicates that the silver coated aluminum particle at the top will take ~1200s (~20min) to sink to the bottom. This presents a major issue with the fabrication of the specimen since typically it takes over 24 hours to allow curing of the sample at ambient conditions (20°C).

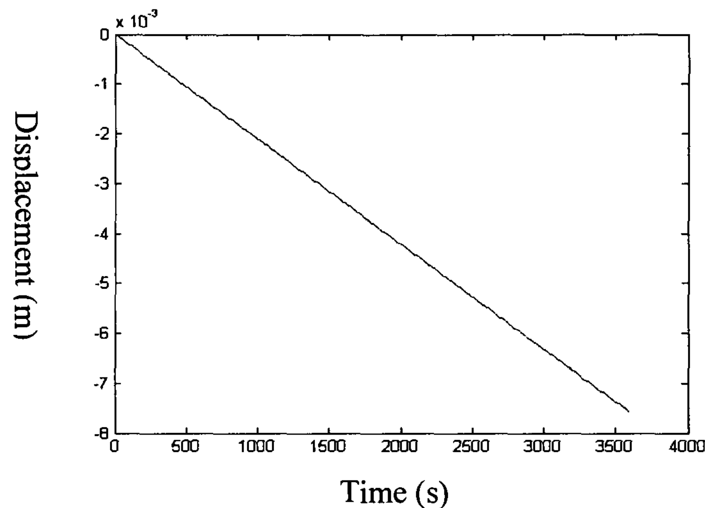

Figure 7 Sedimentation time versus displacement

To prevent particle settle-down, a two-step curing approach is used to process PDMS. The first curing step generates partial cross-linking in the PDMS matrix to increase the viscosity of PDMS. Then, the particles are mixed with PDMS and cured without the sedimentation problem. Because of the high viscosity and limited pre-cross-link, the particles do not sediment appreciably, thus forming a near homogenous composite. The formation of cross-link in the matrix should not be reversible, which will not increase the total curing time (sum of the both steps in the two-step approach) of the PDMS. The time of the first curing step and the time of complete curing at different temperatures are shown in Fig. 8 (the weight of PDMS in each test is 2.0g).

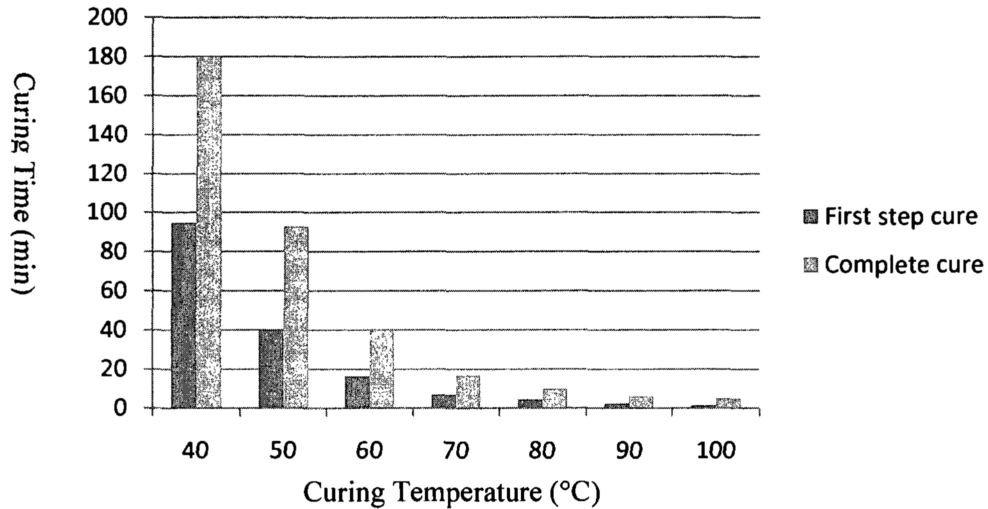

Figure 8 The two-step curing time versus temperature

A simple calculation by applying equation (7) indicates the change of viscosity dramatically affects the length of the sedimentation time. A simple variational study of increasing the viscosity at 50% increments is shown in Fig. 9. It demonstrates that the viscosity is an important parameter that can be manipulated experimentally to affect the sedimentation time. In further work, an experiment will be done to measure the viscosity of PDMS by different curing time to experimentally verify the results.

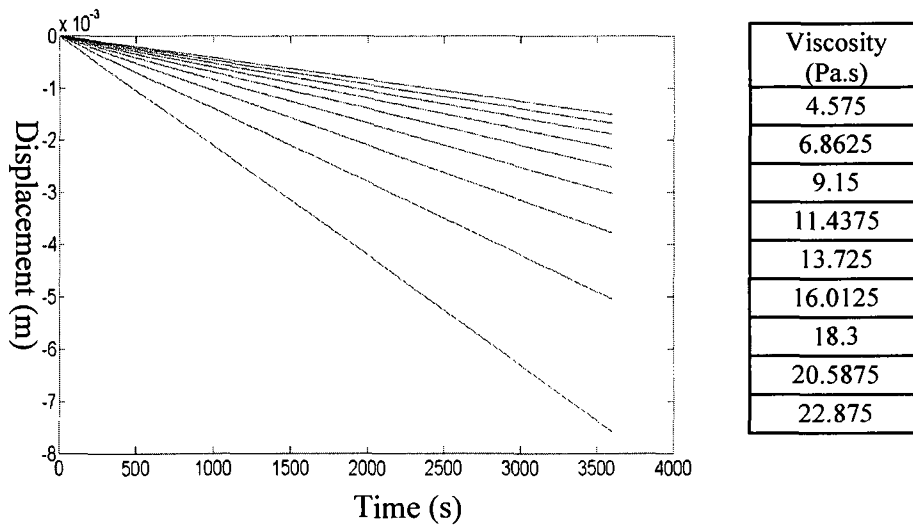

Figure 9 Sedimentation time versus displacement with respect to viscosity

Fig. 10 shows the graph of viscosity versus sedimentation time for the sample holder depth used in the experiments (2.54mm). The sedimentation time increases almost linearly with the increase of the viscosity of PDMS. The graph also shows that the two-step curing approach does help solve the sedimentation problem and resulting in a homogenously mixed sample since the time required for the particle to fully sink to the bottom is now on the order of thousands of minutes versus the tens of minutes required to cure the sample at elevated curing temperature (80°C). It should be noted that single curing steps of curing at higher temperatures are not advised due to the high porosity of the cured composite (since the trapped air bubbles in the PDMS does not have sufficient time to desorb).

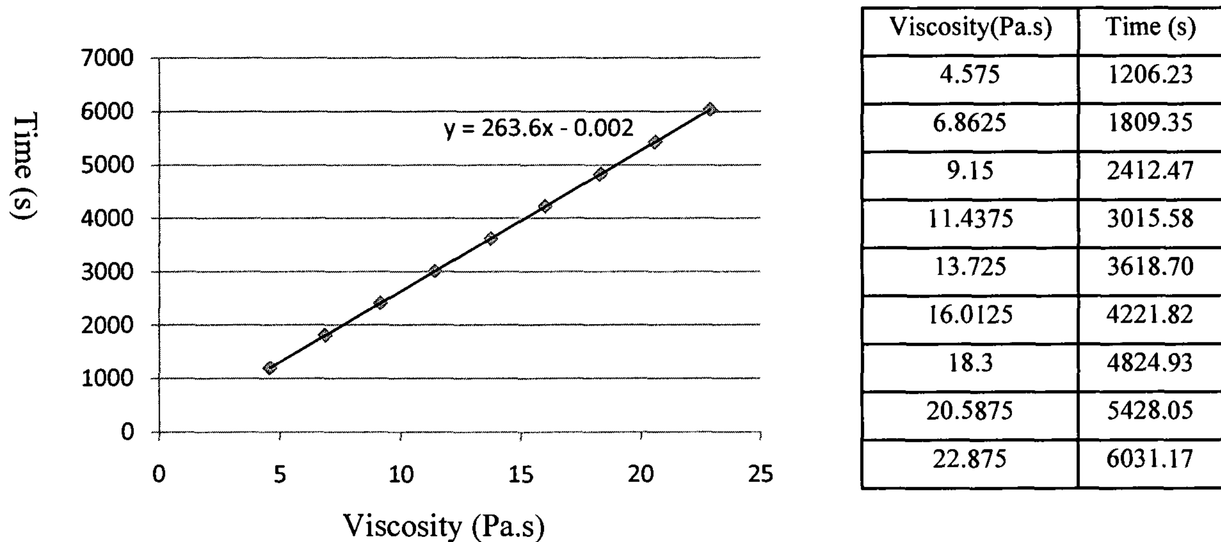

Viscosity(Pa.s)	Time (s)
4.575	1206.23
6.8625	1809.35
9.15	2412.47
11.4375	3015.58
13.725	3618.70
16.0125	4221.82
18.3	4824.93
20.5875	5428.05
22.875	6031.17

Figure 10 Sedimentation time versus displacement

2.3 Resistivity Measurement

Using the two-step curing process, the resistivities of three different metal particles are experimentally derived as a function of mass and volume percentages. The formulas below are used to calculate the mass and volume percentages, respectively.

$$\textbf{Mass percentage} = \frac{\textbf{Mass of particles}}{\textbf{Mass of particles+Mass of PDMS}} \tag{15}$$

$$Volume\ percentage = \frac{Volume\ of\ particles}{Volume\ of\ particles+Volume\ of\ PDMS} \tag{16}$$

According to the dimension of the groove and the measured resistances, the electrical resistivity ρ can be calculated by,

$$\rho = R\frac{A}{l} \tag{17}$$

Where ρ is the electrical resistivity (measured in ohm-meters, Ω cm); R is the electrical resistance of the sample (measured in ohms, Ω); l is the length of the groove (measured in meters, cm); A is the cross-sectional area of the groove (measured in square meters, cm^2).

For the carbon black particle samples, the resistivity versus mass percentage and the resistivity versus volume percentage are plotted in Fig. 11 and Fig. 12, respectively. Fig. 11 shows that for the mass percentage 11%-20%, the resistivity decreases when the carbon particle mass percentage rises. Once the mass percentage is below 11%, the resistance becomes too high to be measured by our instrument (>20MΩ). On Fig. 12, the same data as those in Fig. 11 is converted to volume percentage using the nominal diameters of the particles given by the manufacturer. The trend of data points obeys the power law as usually observed in percolation phenomenon, which means a small change of mass (volume) percentage will cause a large change of resistivity. For example, when carbon particle mass percentage increases from 12% to 13%, the resistivity will increase 7.25×10^4 Ω.cm. That indicates the sensor sensitivity can be guaranteed even with the PDMS barrier.

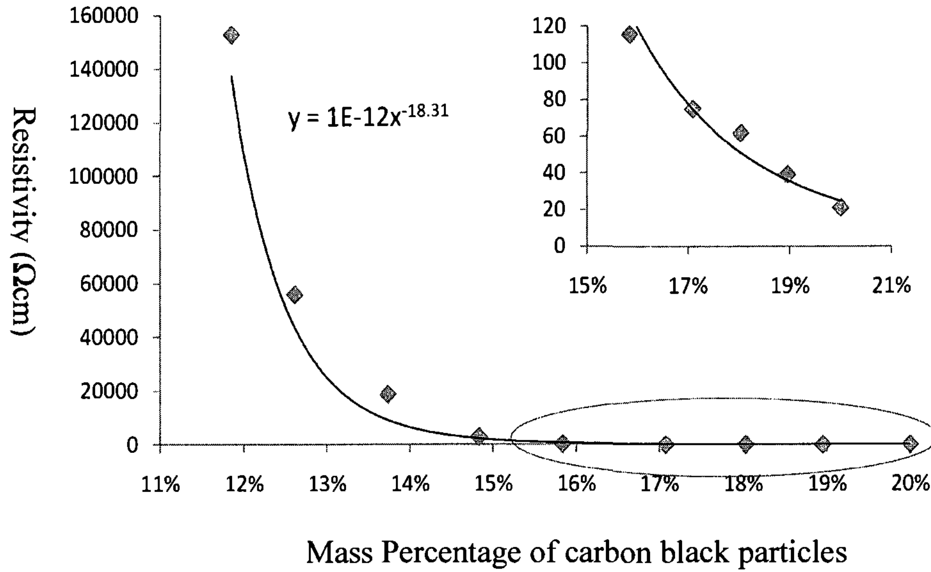

Figure 11 Resistivity versus mass percentage of carbon black particle

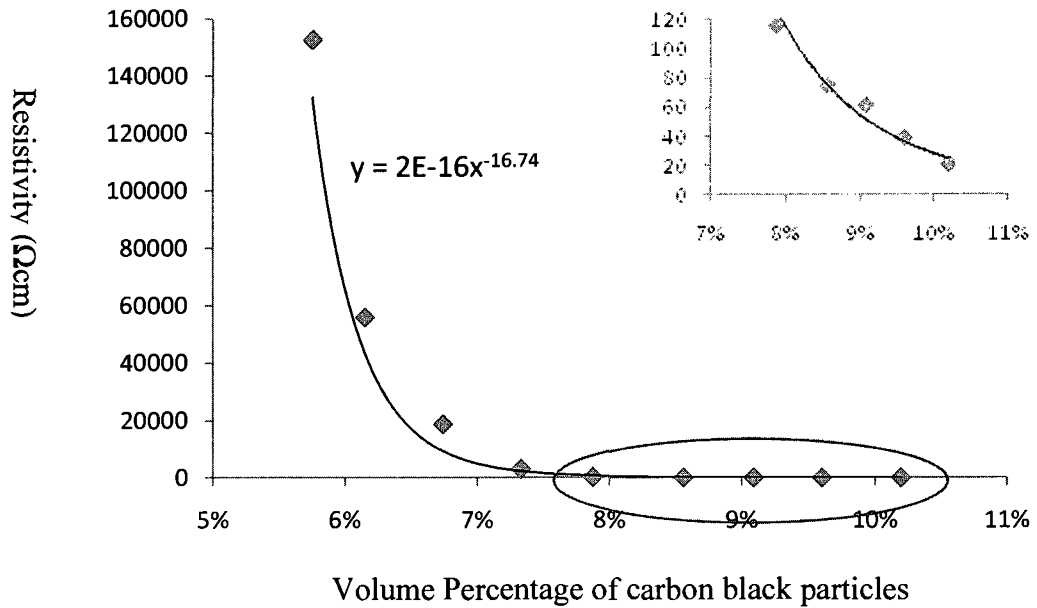

Figure 12 Resistivity versus volume percentage of carbon black particle

Fig. 13 and Fig. 14 show the resistivity versus mass percentage and the resistivity versus volume percentage of silver-coated aluminum particle samples, respectively. The mass percentage is from 50% to 70%, and the interval is 5%. Fig. 11 indicates that there are no measurable resistivity values below 60% percentage. However, once the mass percentage

reach above 60%, the resistivity suddenly becomes extremely low. After reaching 65%, the resistivity stays nearly constant. The power law fit here is not as good as the carbon black particles, which warrants more detailed investigations in the future.

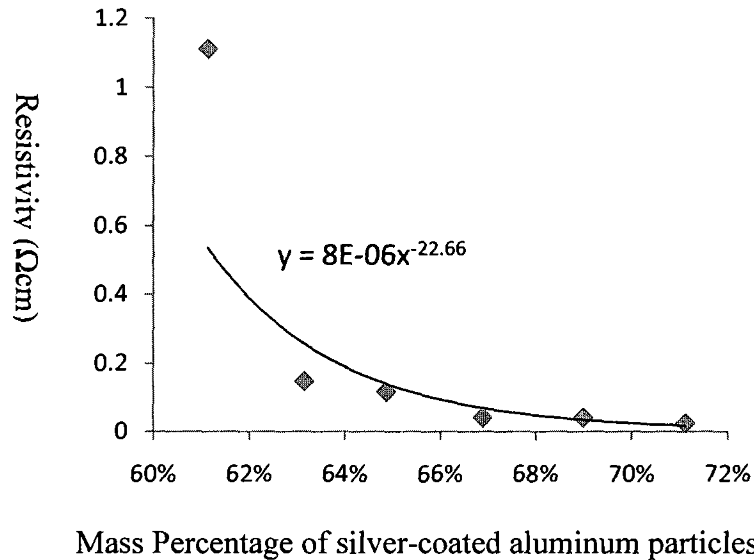

Figure 13 Resistivity versus mass percentage of silver-coated aluminum particle

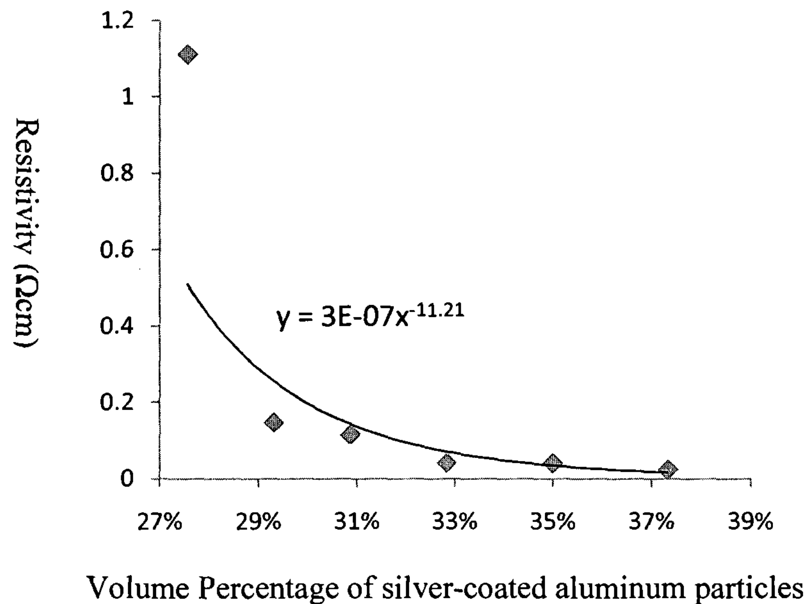

Figure 14 Resistivity versus volume percentage of silver-coated aluminum particle

Fig. 15 and Fig. 16 are graphs of nickel particle composite resistivity versus mass and volume percentage. The mass percentage is from 60% to 80%, and the interval is 5%.

Fig. 15 indicates that there is no measurable resistivity below 60% percentage. However, as the mass percentage reach to 60%, the resistivity value is larger than silver-coated aluminum sample at the same mass percentage. The data points also obey power law thus a large sensor sensitivity value can be expected.

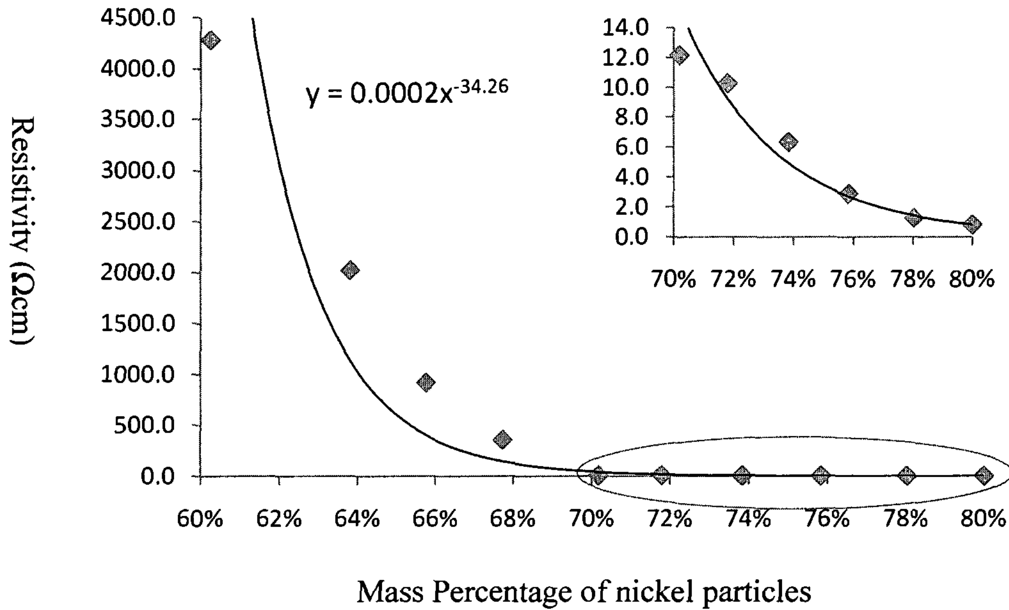

Figure 15 Resistivity versus mass percentage of nickel particle sample

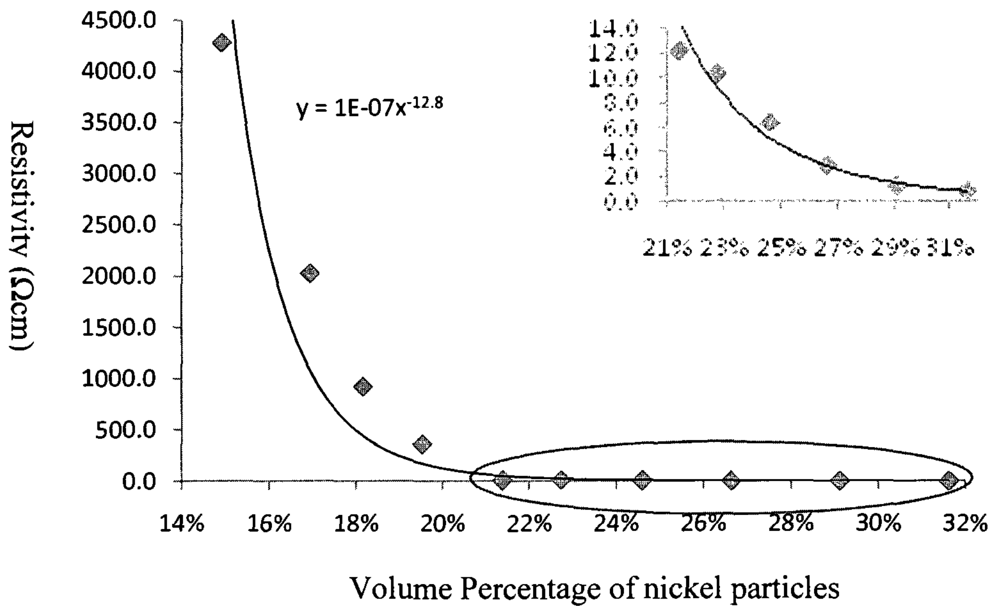

Figure 16 Resistivity versus volume percentage of nickel particle sample

The above experiments show the electrical resistivity of the sensor element relative to metal particles' mass and volume percentages to Polydimethylsiloxane (PDMS) matrix. Three types of particles carbon black, silver-coated aluminum and nickel were tested. The graphs of resistivity versus mass and volume percentage of each of three type particles are shown. The reason of investigating the resistivity by different mass or volume percentage of metal particle is to provide engineering guidelines in future corrosion sensor development. It also presents the solution to the sedimentation problem of metal particles in liquid PDMS in mixture and curing process. It was shown that manipulating the viscosity of the PDMS is a practical method in eliminating sedimentation.

CHAPTER 3

REMOVAL OF OXIDE ON METAL PARTICLES FOR FABRICATING MEMS-BASED CORROSION SENSOR

3.1 Introduction

As mentioned in Chapter 1, the oxide of metal particles is often disadvantageous for the electrical conductivity and sensitivity of the corrosion sensor. Due to the relatively large surface area to volume ratio of nano- and micron-sized particles, any changes in the surface property will dominate the electrical characteristics of the metal particle polymer composite.

This chapter provides an oxide removal approach based on the wet etching process. Diluted hydrochloric acid is applied to react with the oxidized coating of the metal particles (e.g. nickel). The resulting chemical reaction is a soluble metal chloride solution that is repeatedly diluted and dumped by IPA (Isopropyl alcohol) solvent, which prevents re-oxidization of the metal particle while immersed in the solution. The remaining pure metal particles are then collected and baked and then used in the sensor fabrication.

3.2 Experiment

In this experiment, nickel particle is used to do the preliminary test. Nickel oxide reacts with hydrochloric acid easily. The generated nickel chloride is soluble in water. Moreover, nickel chloride does not react with IPA solvent, which means the nickel chloride is rinsed out without further reaction to the bare metal particles. Nickel particles (-325mesh, typically 99.8% <metals basis>) used in the experiment are sourced from Alfa Aesar® Inc [25].

The first step is to dilute the hydrochloric acid (wt 36.5%; EMD Chemicals, Inc.) to a 100mL solution of 0.01mol/L concentration with de-ionized water. Then, 0.5g of the

nickel particles are added in the solvent. The nickel oxide reacts with hydrochloric acid, which has the following chemical equation (1):

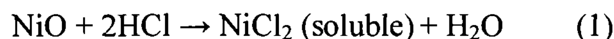

$$NiO + 2HCl \rightarrow NiCl_2\,(soluble) + H_2O \qquad (1)$$

$$Ni + 2HCl \rightarrow NiCl_2\,(soluble) + H_2\,(gas) \qquad (2)$$

Initially, the color of solution will change to green gradually, which is the color of $NiCl_2$. After 15minutes, there are bubbles coming out from the bottom, which means the hydrochloric acid starts reacting with the pure nickel and the gas is hydrogen molecules, as indicated in equation (2). The reaction is sustained for 90min in order to be sure of removing all nickel oxides. Then the nickel particles are prepared for rinsing, drying, and collection.

The key to success in this experiment is to prevent the pure nickel particles to be exposed in the air and be oxidized again. A glove box is set up to achieve the necessary protective environment. A sealed glove box with bleeding valve is filled up with nitrogen gas (concentration 99.5%, welder's grade). The dumping and rinsing of the residual solution by using IPA solvent 4 times is used to dilute and remove the nickel chloride solution. Then the particles are poured on a filter paper and baked on the hotplate at 80°C for 1 hour in the glove box to vaporize the residual IPA mixure with nickel particles. The mass of collected nickel particles is about 0.22-0.31g, representing roughly 50% mass loss. Because the process is operated in a nitrogen gas environment, these nickel particles cannot be re-oxidized. The deoxidized particles are then mixed with PDMS at varying mass percentages to measure the resistivity of the samples and compare to the same mass percent nickel particle samples to investigate the quality of the de-oxidizing experiment.

In this step, the same PDMS (Sylgard® 184) is used as in previous experiments. When mixing the PDMS, typically, the mixture ratio of PDMS monomer and curing agent is 10:1 by mass. After the PDMS is mixed, it is blended with the etched nickel particles. The density of pure nickel is 8.908g/cm^3, which is higher than the density of PDMS (~1.03g/cm^3). These particles will settle down at the bottom when mixing, which causes inaccurate resistance measurement of an assumed homogenous composite. In order to improve the accuracy of the material characterization, it is necessary to mix up PDMS with the anti-sedimentation method described in the previous chapter..

For the deoxidized nickel particle sample, the resistivity versus etching time is plotted in Fig. 17, which shows that, at mass percentage of 70%, with the etching time 15-90min, the resistivity decreases when the etching time increases. Once the etching time is above 90min, the resistance becomes fairly constant. When the etching time reaches to 90min, sample resistivity decreases to 0.66Ωcm.

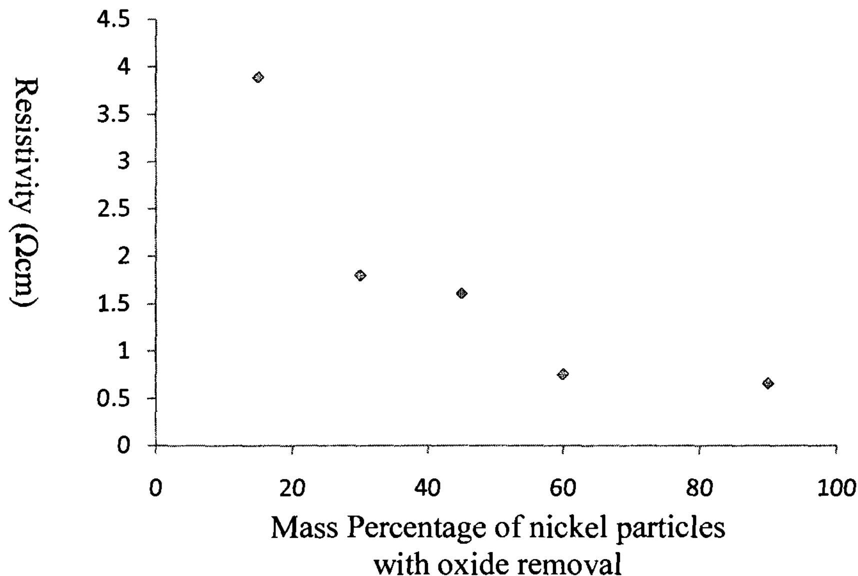

Figure 17 Resistivity versus mass percentage of nickel particles with oxide removal process

Fig. 18 and Fig. 19 show the resistivity versus mass percentage and the resistivity versus volume percentage of nickel particle without de-oxidation, respectively. For Fig. 18, the mass percentages are in the range from 60% to 80%, and the interval is 2%. Fig. 18 indicates that there is no measurable resistivity below 60% percentage. However, for the samples with oxide removal, at 70% (etched by only 15min) the resistivity decreases down to 3.89Ωcm. On the other hand, at 70% for particles that was not etcched, the resistivity value is 11.9Ωcm, which is much higher comparing to the resistivity of the sample with oxide removal process at the same percentage, 3.89Ωcm. This result demonstrates that oxide removal process do improve the electrical transduction of the composite. Fig. 19 shows the equivalent plot of the resistivity versus volume percentages from 14% to 32%.

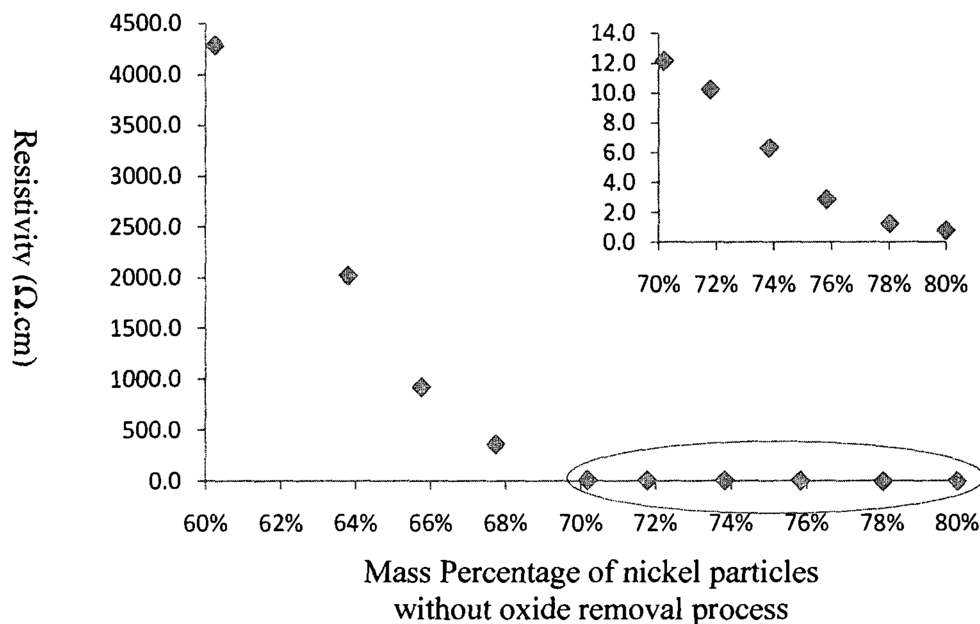

Figure 18 Resistivity versus mass percentage of nickel particles without oxide removal process

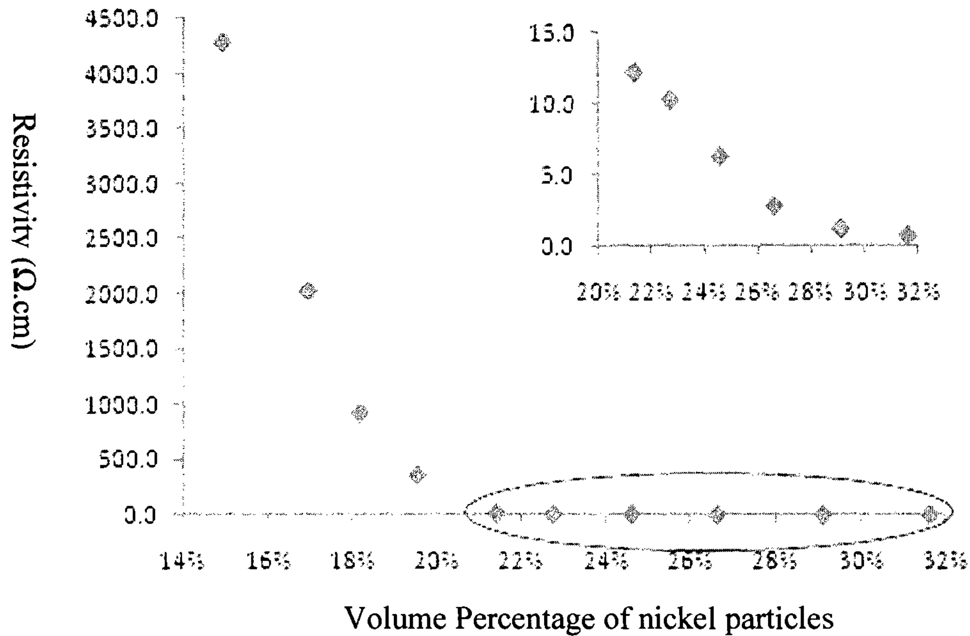

Figure 19 Resistivity versus volume percentage of nickel particles without oxide removal process

3.3 Results and Analysis

This chapter provides an approach to solve the oxidation problem of metal particles. Chemical wet etching is the main process applied in this approach. After de-oxidization, these fresh metal particles are rinsed and baked in nitrogen gas environment to prevent oxidizing again. Then the conductivity of nickel composite sample is investigated. The comparison to nickel particle sample without de-oxidation are presented, demonstrating that the deoxidized nickel performs better in terms of lower conductivity.

CHAPTER 4
DIRECT POLYMER PATTERNING ON SUBSTRATE TECHNIQUE AND ITS MODIFIED APPROACH

4.1 Introduction

This chapter describes the basic Direct Polymer Patterning On Substrate Technique (DPPOST) process and a modified process currently under development to provide higher robustness in the fabrication process, with the goal of achieving near 100% patterning yields. The patterning of soft-polymers and elastomers has gained interest in the last decade as the material of choice for lab-on-the chip applications; i.e., forming micro-fluidic and bio-reactor chambers. Recently, a lithographically compatible patterning method for soft-polymers and elastomers have been demonstrated by using SU-8® hard polymer resists as robust lift-off molds. This patterning technology, DPPOST, has the ability to form a wide range of structural features found in MEMS, from tens of millimeter structures to micrometer level resolutions. It has been used to embed nano-particles, such as carbon-black (~45nm mean radius) and metal particles, and allows lithographic alignment of electrodes on micro-fluidic channels previously not possible with soft-lithography fabricated PDMS devices. The modified-DPPOST process uses conformal coating of Omnicoat™ nano-films to provide a barrier between the SU-8® and the patterned polymer, hence reducing stiction during the release process.

Polymers are widely used materials in MEMS due to their unique properties, including high chemical inertness, high elongation ratio, surface properties, proper thermal/electrical insulation and stability, and low Young's modulus [26]. Spin-on polyimide (PYRALIN®) and SU-8® polymers have been used to provide tailored capabilities due to their inherent properties [27]. In addition, vapor deposited polymers,

such as parylene, have found widespread usage as conformal protective coatings and fluidic seals [28].

Despite the availability of polymer materials for MEMS fabrication, patterning polymers such as silicone elastomers has remained a common problem [26]. Silicone is extremely resistant to reactive ion, oxygen plasma, and chemical etching techniques. It is also difficult to pattern silicone directly with photolithography without significantly degrading its high elongation ratio and mechanical compliance properties [29]. The current methods of patterning soft polymers, like silicone-based materials, using different variations of soft lithography generally do not yield high alignment accuracies or full wafer patterning with consistent dimensional stability of the patterned features [26, 27]. Recently, a surface micromachining technique, utilizing a dissolvable photoresist (AZ4620) mold and squeegee, for patterning poly-dimethylsiloxane (PDMS) on solid substrates has been developed by K.S. Ryu [28, 29]. However, patterning highly viscous polymers with the typical dissolvable photoresists is difficult due to the squeegeeing steps. A method of full wafer patterning technique would also be desirable.

In the past few years, Huang et al. has successfully developed a robust method to pattern silicone polymer on substrate directly, which is called Direct Polymer Patterning On Substrate Technique (DPPOST) [26]. By using DPPOST, 25μm square patterns have been achieved. Other advantages of DPPOST include photolithographic alignment accuracy, a high dimensional stability, full wafer patterning, and parallel processing found in traditional MEMS fabrication [26]. The first MEMS device—chemical vapor sensor applying the DPPOST technique has been presented and tested [27, 29, 31]. In order to improve the performance of this type of sensor, miniaturization of individual

sensor elements is the critical aspect. Using micro-fabrication technology, the sensor density can be increased further to provide data redundancy for statistical analysis [12]. However, miniaturization of polymer based sensing devices has been a challenging task due to the lack of appropriate wet/dry etching methods, as mentioned previously. In order to prepare these devices, researchers have used approaches such as immersion [12], spray [12], and spincoating [13] of the polymer/carbon black solution onto substrates. The overall dimensions of the resulting devices are restricted to the dimension of the substrate (or diced pieces of the substrate).

As described by Huang et al., the DPPOST technique is parallel processing and surface micromachining compatible, while the ultimate line-width should only be limited by the lithographic resolution of the patterned materials. The percentage of complete patterns on the whole wafer is high (~90%), but not 100 percent. Other issues experienced include lift-off sensitivity to patterns with high aspect ratios. The main reason may be the stiction between the SU-8® mold and the patterned polymer, where higher aspect ratio patterns increases such damaging stiction forces.

The focus of the current modified DPPOST work is to reduce the stiction problem discussed above. An extra deposition of Omnicoat™ (MicroChem Corp) is used to separate SU-8® and polymer patterns. The most important parameter in the modified approach is the deposition and etching rate of the Omnicoat™, which controls the thickness and roughness of the lift-off layer.

4.2 DPPOST Fabrication

The DPPOST fabrication technique is similar to the lift-off technique that is commonly employed in MEMS fabrication of metals. The key difference is that the

conformally coated polymer, as oppose to thermally deposited metals, is separated from the patterning area through mechanical polishing. The DPPOST uses the SU-8® (MicorChem) as the photo-lithographically patterned sacrificial layer for lifting-off the top coat of the conformally deposited polymer. As part of the standard lifting off procedure of the SU-8®, a thin layer of Omnicoat™ is used to act as the sacrificial layer between the substrate and the SU-8®. Omnicoat™ is an organic compound that also acts as adhesion promotion for SU-8®. It is nominally 15nm thick and can be easily removed by oxygen plasma, Remover PG®, or TMAH based developers [23].

SU-8® is a negative photoresist commonly used in the MEMS fabrication of high-aspect ratio microdevices. The advantages of SU-8® over other types of photoresists include high aspect ratio, hydrophobic surfaces, high dielectric constant, and temperature stability; yielding deep robust structures [26]. SU-8® is also easy to spin onto a wafer and can range in thickness from <1um to >200 um in a single spin coat, depending on the specific type of SU-8® used.

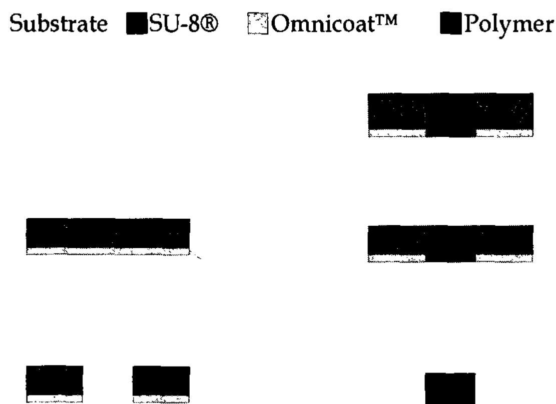

Figure 20 The process flow of DPPOST

The general process flow of the DPPOST technique is shown in Fig. 20. First, a thin dissolvable Omnicoat™ is deposited on a silicon wafer. Typically, the Omnicoat™ is

spin-coated onto the wafer at a speed of 3000rpm. Then it is baked on hotplate at 200°C for 1 minute. Then, by using SU-8® 2025 spin-coated at 3000rpm a film thickness of about 30μm is achieved [23]. The standard 2-step soft bake for the SU-8® at 65°C for one minute and 95°C for five minutes is then used prior to exposure.

To pattern the SU-8® the wafer is exposed on a Karl Suss MA-150 top-side aligner. The required total energy of SU-8® for this thickness is 150 mJ/cm^2 [26], which corresponds to 23.1 seconds of exposure at 6.5 mW/cm. In accordance with the manufacturer's recommendation, a UV filter is used to eliminate UV radiation below 350 nm which eliminates cracks in the SU-8® and allows better sidewall definition [26]. The adjustments on exposure time for using the filter and patterning on a silicon wafer are an additional 40% and 50% respectively [26]. The total exposure time used is thus 48.5 seconds.

After exposure a Post Exposure Bake (PEB) step is required at 95°C for five minutes [26]. The SU-8® developer composed of 1-Methoxy-2-Propanol Acetate is used as a wet etch and the wafer is dipped in the bath for approximately five minutes. If the SU-8® is not developed enough the pattern would turn white as if it were frosting when rinsed with IPA. The wafer can be dipped back into the developer until it is fully developed. The wafer is then etched in oxygen plasma to ash the exposed Omnicoat™, which is done for five minutes with a gas flow rate of 80sccm and RF power of 250W.

As part of the patterning process for the silicone carbon-black sensor, typically the 10:1 mass ratio of RTV615A to RTV615B, respectively, is used. This elastomer is very similar in mechanical and electrical property to PDMS and is used here simply for direct comparison with previously published works. Carbon-black particles with average sizes

of 0.042 microns is then mixed with the silicone compound at 20% by weight and then applied to each individual SU-8® mold using a glass slide. The polymer takes approximately 24 hours to completely cure. A diamond abrasive pad is used to polish the surface of the wafer and remove the excess top coated polymer. The wafer is then dipped in a bath of Remover PG® (MicroChem) heated to a temperature of 130°C. The remover PG dissolves the Omnicoat™ layer and allows the SU-8® layer to lift off. By applying the DPPOST technique, 25μm square patterns are obtained. Smaller patterns have also been fabricated using DPPOST [1].

However, sometimes the lifting-off process of the SU-8® for DPPOST has problem as illustrated in Figure 21. The figure shows an example that some parts of the element are torn off and the sidewalls are not sharp. The reason for this is that the sidewalls of the elastomers stick with SU-8®. Sometimes residual SU-8® remains on the edge of patterns while parts of patterns have been stripped off after development. This is especially true when the side-walls of the SU-8® are not properly prepared (negative side wall slopes and cracks) and the RTV615 is overly cured, which results in enhanced stiction between the elastomer and the mold. This can be avoided with well controlled SU-8® patterning and the curing of the deposited polymer. Ideally the DPPOST patterning should be designed to be more robust and tolerant of fabrication steps.

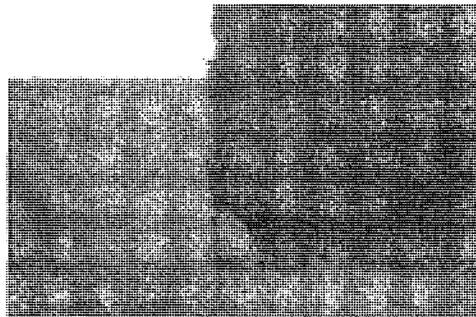

Figure 21 Example of lift-off problems at 40X magnification

4.3 Modified Approach of the DPPOST

In an attempt to correct the problems caused by the lift-off step in DPPOST, a second method is developed to allow the silicone elastomers to adhere only to the substrate not to the SU-8®. A proposed method is to apply an extra layer of Omnicoat™ onto the pattern over the SU-8® layer. Ideally, this layer would create a separation region between SU-8® and the deposited polymer, allowing ease of lift-off.

The process flow of the modified DPPOST is shown in Fig. 22. For the procedure of modified DPPOST, the protocol of the original DPPOST is repeated until the application of the silicone elastomer material to the pattern. Instead of following with the normal DPPOST steps, an extra layer of Omnicoat™ is spun onto wafer at a 3000rpm for 30 seconds. The wafer is then baked at 200°C for 1 minute. From this point on the modified process is identical to the original DPPOST.

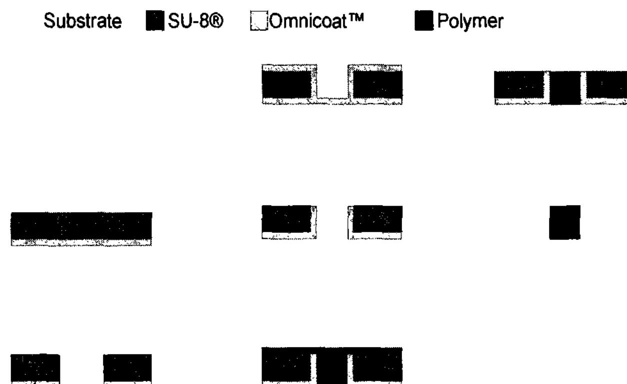

Figure 22 Process flow of modified method for the DPPOST

To achieve good quality in the resulting structure patternedl, maintaining the consistent thickness of Omnicoat™ on vertical sidewall is the key to the modified

approach. This thin layer not only decides the SU-8® lift-off, but also decides the quality of patterns as compared to the mask image. In the first series of experiments, the extra Omnicaot™ layer was spin-coated onto the surface and then etched by oxygen plasma, both of which directly determine the thickness and roughness of the vertical Omnicoat™ layer; further affecting the final patterns. By spin-coat, the Omnicoat™ solution should have been deposited on the surface and covered each individual hole-pattern. However, that was not the case. Fig. 23 (top side down image, by Environmental Scanning Electron Microscope) demonstrates the cross section of 25μm width SU-8 lines patterned on substrate, with spin-coated Omnicoat™ between SU-8® patterns. The Omnicoat™ cannot fill up the hole-patterns completely while clogging up the top side. It cannot cover the SU-8® pattern surface smoothly. The reasons for this phenomenon might be the gap size is too small to be filled by Omnicoat™ solvent; or the subsequent bake step heterogeneously evaporated the Omnicaot™ inside, reducing its volume.

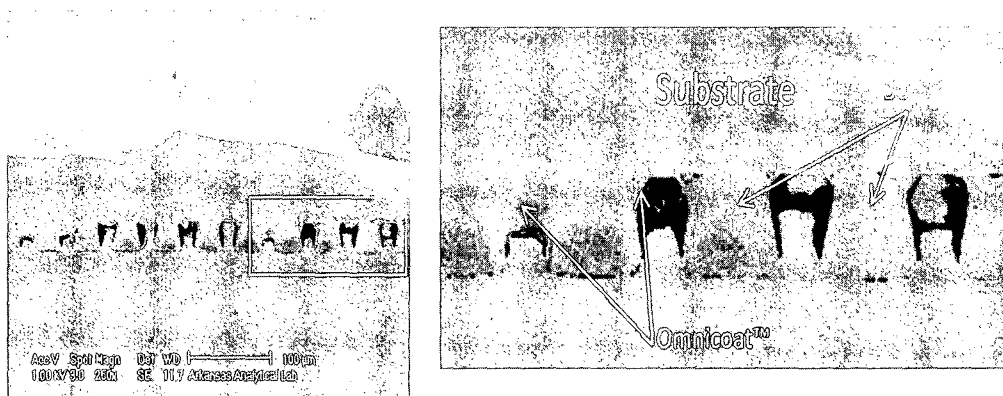

Figure 23 Cross section of 25μm width SU-8 lines patterned on substrate (upside down), with spin-coated Omnicoat™. Left: Image of cross-section of SU-8® patterns; the width of patterned lines is 25μm. Right: the magnified image of the framed area.

4.4 Oxygen Plasma Etching Rate Test

Another factor that affects the vertical layer is the oxygen plasma etching. Typical oxygen plasma etching in ashers is anisotropic (non-directional). This means that the vertical layer of the Omnicoat™ may be removed by the plasma etching step. Thus, a better knowledge of the deposition and etching process of the Omnicoat™ is required for properly developing the modified DPPOST process. Thus, an etch rate experiment is performed to find the etch rate and coating thickness of the Omnicoat™. The process flow of the test experiment is shown in Fig. 24.

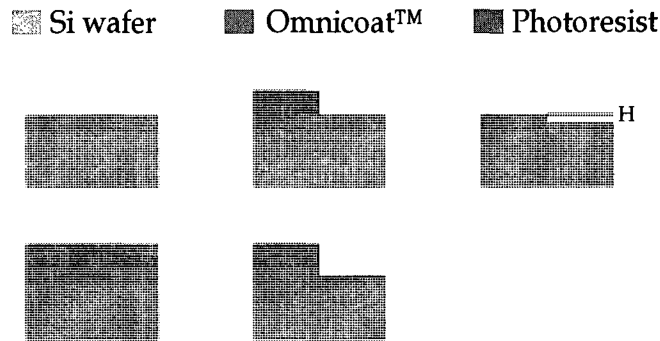

Figure 24 Process flow of testing oxygen plasma etching rate

First, a 100mm silicon wafer is cut into 10mm x 10mm chips by dicing saw, spin-coat with Omnicoat™ and AZ 4620 positive photoresist on each chip. The spinning speed for the Omnicoat™ and photoresist are both 3000rpm, which yields film thicknesses of roughly 15nm and 9μm, respectively. Then, the chips are exposed and developed to remove half side of the photoresist, leaving the Omnicoat™ partially exposed. After development, they are ashed in oxygen plasma (APE 110 General Purpose Barrel Plasma Unit) sequentially with a gas flow rate of 80sccm, 450mtorr, and RF power of 250W. The etching time is set from 0.5min to 5.0min in 0.5 min intervals. The masks for the etched chips are then stripped in acetone.

Atomic force microscope (Multimode in Pico-force Mode, Vecco Corp.) is used to measure the height difference between exposed and unexposed part of each chip. Fig. 25 shows AFM images by etching 0.5min, 2.5min, and 5.0min respectively.

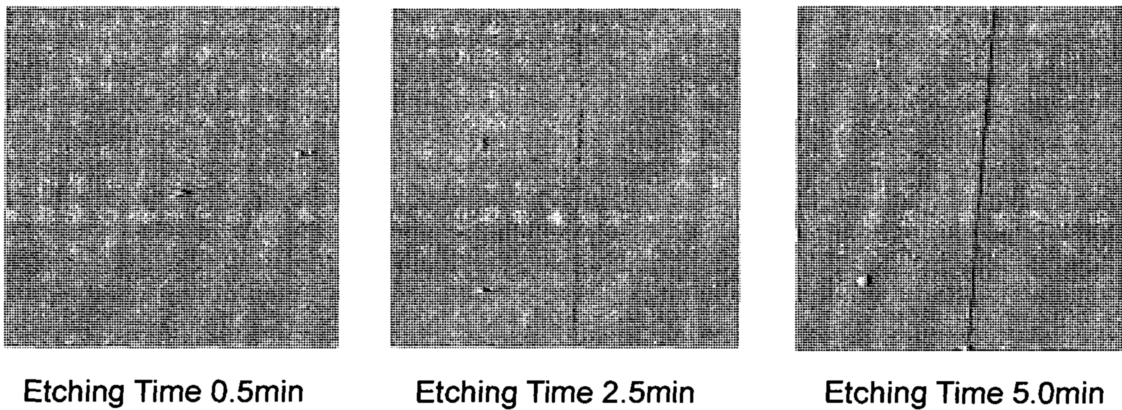

Figure 25 AFM images of chips etched by different time

Plotting the etching time versus depth, the oxygen plasma etching rate for the Omnicoat™ can be obtained, as shown in Fig. 26, which is 2.4 nm/min. the value is much smaller than expected and this may be due to the slow etch rate of the asher used (since the manufacturer's specifications listed 30 seconds etch time as typical). The slope of etching rate plot does not pass the origin and is shifted upward. This may be due to the asher, which starts the etching timer countdown only after attaining stable plasma. Thus, the actual etching time is longer than set time. However, the etch rate should be correct since the slope is invariant of the initial etching conditions.

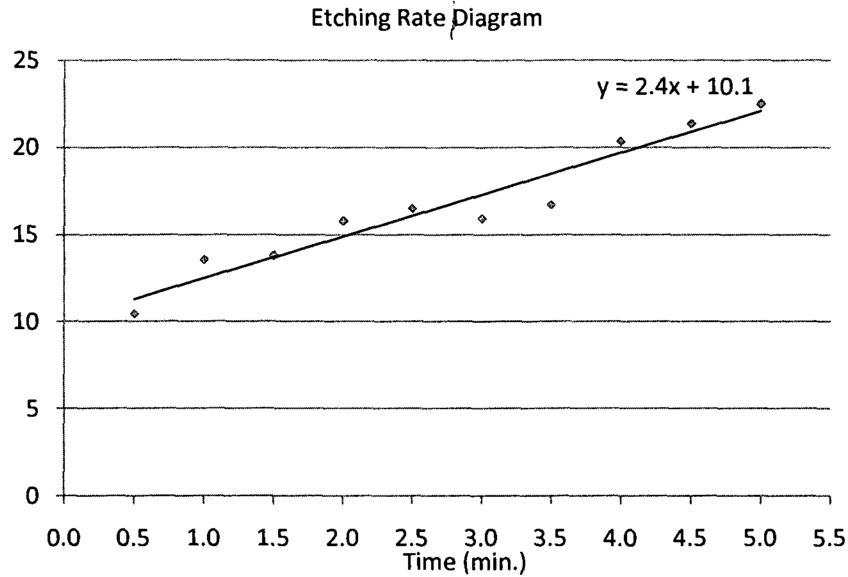

Figure 26 Oxygen plasma etching rate using APE 110 General Purpose Barrel Plasma Unit

Currently, we are repeating the experiment using RIE-based oxygen plasma to provide faster etching, better process control, repeatability, and directional etching. Fig. 27 illustrates the etching rate of the Omnicoat™ due to the RIE (Plasma-Therm SLR SERIES). For comparing with the APE110, the same setting power is used for this RIE-based asher. From the graph, the Omnicoat™ is almost eliminated in 1 minute. It shows that the RIE-based oxygen plasma provides faster etching. Key future experiments include the determination of the directional etching of the RIE as opposed to the conformal characteristics of the asher, which is needed for the improved DPPOST. Other possible side-wall preservation methods may include techniques similar to DRIE.

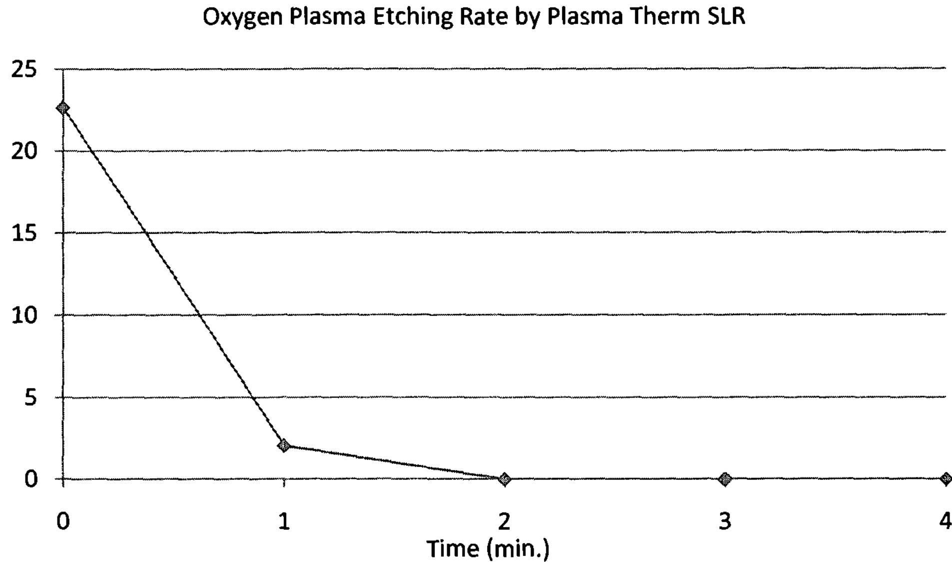

Figure 27 Oxygen plasma etching rate using Plasma-Therm SLR. The vertical axis is the Omnicoat™ film thickness in nanometers.

4.5 Optimize the Modified DPPOST Technique

Due to the problems from spinning-coat Omnicoat™ in the modified DPPOST, two methods of using vapor priming to deposit Omnicoat™ is currently ongoing and summarized here. Vapor priming methods often provides evenly deposited surfaces and that vapor molecule can pass through smaller gap comparing with liquid coating. It can also reduce the amount of deposited materials used. Thus, we started to investigate vapor priming system as a way to provide the required conformal second Omnicoat™ layer. The first method employs a bubbler generator connected with a flask filled with Omnicoat™. Nitrogen is bubbled through the Omnicoat™ and its vapor is carried into the deposition chamber, where it coats the wafers. The setup of vapor priming is illustrated in Fig. 28.

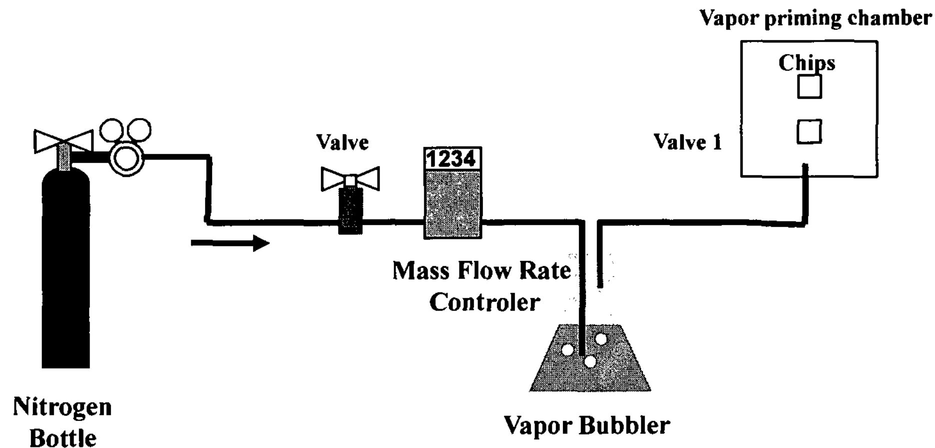

Figure 28 Vapor priming illustration

Another type of vapor priming is called thermal vapor priming, which employs an evaporated vapor from a reservoir of liquid Omnicoat™. The Omnicoat™ is heated to create vapor, which is then used to coat the wafer placed at a standoff distance above the liquid surface. An illustration of this method is shown in Fig. 29. The chips are put on a flat surface which is totally seal in the reservoir. The reservoir is heated up to 60°C on a hot plate. The temperature is controlled manually by a thermometer. Before the chips are put into the reservoir, they are preheated up to 120°C in order to prevent Omnicoat™ condensations on the chip. Chips are vapor-primed from 15 to 60 minutes at 15 minute intervals. A scalpel (X-acto knife) is used to scratch on the chip. The knife removes the soft Omnicoat™ polymer and provides a step for height measurements, performed using AFM.

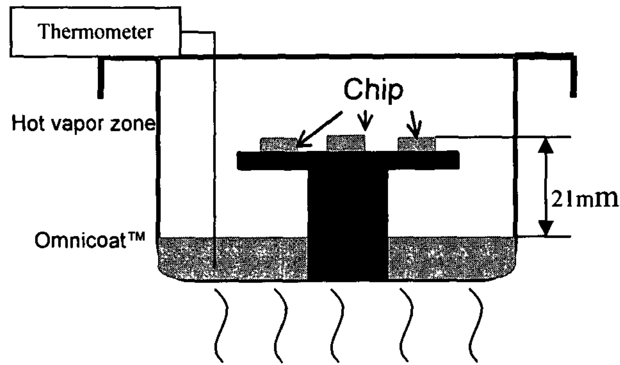

Figure 29 Thermal Vapor Priming illustration

Fig. 30 shows the thickness increment by increasing time. The growth of the thickness is very slow, even after one hour the thickness is only 5.837nm. This demonstrates that the thermal vapor priming can be applied to grow nano-films of Omnicoat™, which contributes to the deposition of Omnicoat™ on the sidewall.

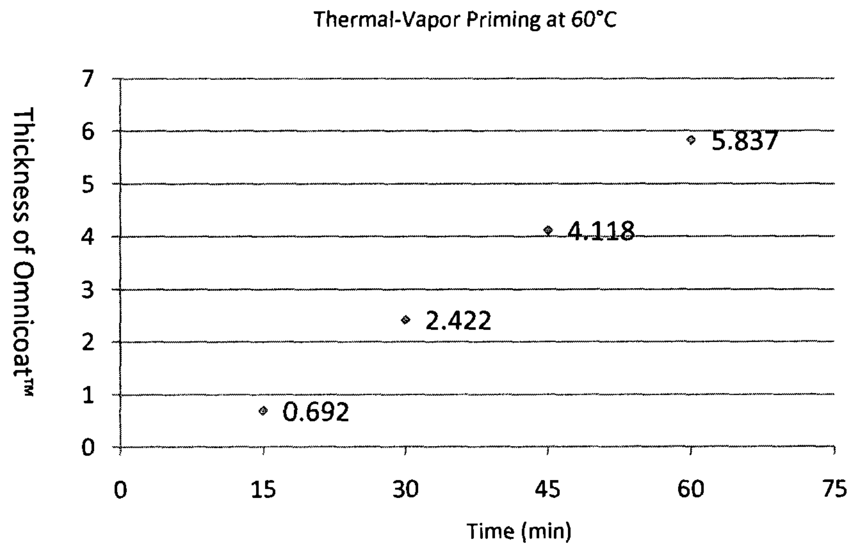

Figure 30 Thermal Vapor Priming Thickness vs. Time

This chapter presents the Directly Polymer Patterning On Substrate Technique (DPPOST) for MEMS fabrication. Additionally, the modified method of the DPPOST is also demonstrated here with the intent of improving the fabrication yield toward 100%.

The modified approach requires a double coating of the Omnicoat™, which serves as the barrier material between the substrate, SU-8®, and the deposited polymer. In order to optimize the modified DPPOST, experiments of oxygen plasma etching rate has been done to provide accurate etch rate of the Omnicoat™. The etching rate is 2.3996nm/min by using APE110 asher, which is smaller than expected, but most likely is due to the asher equipment used. It was found that the RIE-based asher provides more efficient etching comparing with the APE110 asher. Thermal vapor priming to grow Omnicoat™ layer is also demonstrated. The interesting result is that the thickness of the layer is very thin at 5.837nm for an hour at 60°C in the reservoir.

Further work will focus on the new pattern techniques, vapor priming and thermal vapor priming, in order to obtain smooth and evenly deposited layer of Omnicoat™. Systematic experiments is needed to test the relation between deposited thickness and the mass flow rate of nitrogen for the first type of vapor priming; for the second, thermal vapor priming, the relationship between deposited thickness, the vapor priming time, temperature, and the standoff location needs to be known. These characterization efforts are currently on-going.

CHAPTER 5
CONCLUSIONS AND FUTURE WORK

5.1 Conclusions

The electrical resistivity of metal particle to Polydimethylsiloxane (PDMS) matrix mass percentages was investigated. Three types of particles: carbon black, silver-coated aluminum and nickel were used. The metal particles used were micron-sized instead of the nanometer sized carbon particles, resulting in the sedimentation of metal particles during sensor element fabrication. It was shown that the viscosity of the PDMS can be manipulated for eliminating sedimentation through a two-step curing process.

In order to eliminate the native oxide layers on metal particles prior to mixing with PDMS, an approach to solve the oxidation problem of metal particles has been demonstrated. Chemical wet etching is the main process applied in this approach. After oxide removal, native metal particles are rinsed in IPA and baked in N_2 gas environment to prevent re-oxidization. Then the conductivity of nickel composite sample is investigated using the above approach with HCl. The comparison to nickel particle sample with and without etching are presented and yielded significantly better conductivity values. It proves that the developed oxide removal method is applicable to nickel particle and theoretically a viable technique for other metal particles.

Other type of metal particles such as aluminum, stainless, and titanium will be tested in the further work. A quick set of corrosion test has been done to investigate the corrosion rate of metal particles in PDMS matrix and will be used to detect the corrosion rate.

In the last chapter the modified method of the DPPOST has also been demonstrated with the intent of improving the fabrication yield toward 100%. The modified approach requires a double coating of the Omnicoat™, which serves as the barrier material between the substrate, SU-8®, and the deposited polymer. In order to optimize the modified DPPOST, a test of oxygen plasma etching rate has been done to provide accurate etch rate of the Omnicoat™. The etching rate is 2.3996nm/min by using APE110 asher, which is smaller than expected, but most likely is due to the asher equipment used. The RIE-based asher provides more efficient etching comparing with the APE110 asher. Thermal vapor priming to grow Omnicoat™ layer is also presented in the paper. The interesting result is the ability to coat nano-films at a very slow rate using this method (5.8 nm/hour).

5.2 Future Work

To achieve the development of the MEMS corrosion sensor, there are five main experimental research that must be done next.

First, investigate oxide removal for other types of metal particles, such as aluminum, copper and steel. For the aluminum particle, we probably will use hydrofluoric acid to etch alumina due to the high etch rate of most acids on the native aluminum itself. For copper particle, acetic acid can be used to remove oxide without etching copper.

Second, investigate the gas diffusion by different gases such as air, oxygen, and carbon dioxide. This is the most important investigation because it determines whether the corrosion sensor work in real experiment.

Third, experimental measurements of sensor characteristics with different metal particles (Nickel, silver-coated aluminum, Aluminum, copper, iron, and stainless steel) in

Electrical Resistance (ER) and Electro-Chemical Noise (ECN) will be done to correlate the corrosion rate to changes of electrical resistivity of the composites.

Fourth, the coupon of sensor element materials with different metal particles will be subjected to salt spray test in term of the ASTM B117 standard, demonstrating the concept of metal particle polymer composite as a MEMS corrosion sensing element. The salt spray tests will be used to quantify corrosion sensor morphological, electrical, and dimensional characteristicsxz.

Last, further work will also focus on the new pattern techniques, vapor priming and thermal vapor priming, in order to obtain smooth and evenly deposited layer of Omnicoat™. Systematic experiments are needed to test the relationship between deposited thicknesses and the mass flow rate of nitrogen for the first type of vapor priming; for the second, thermal vapor priming, the relationship between deposited thickness, the vapor priming time, temperature, and the standoff location needs to be known. These characterization efforts will be done in my future study.

REFERENCES

[1] Jones, Denny (1996). Principles and Prevention of Corrosion (2nd edition Ed.). Upper Saddle River, New Jersey: Prentice Hall. ISBN 0-13-359993-0.

[2] Corrosion of Glass, Ceramics and Ceramic Superconductors. Edited by: D.E. Clark, B.K. Zoitos, William Andrew Publishing/Noyes, 672pp. (1992).

[3] Roberge, P.R., (2000) Handbook of Corrosion Engineering. McGraw-Hill, New York

[4] Callister, W. D., (1994) Material Scinece and Engineering, An Introduction. John Wiley&Sons Inc. New York.

[5] Huang, Adam, Victor Tak Sing Wong, and Chih-Ming Ho. "Silicone Polymer Chemical Vapor Sensors Fabricatired by Direct Polymer Patterning on Substrate Technique (DPPOST)." Sensor and actuator B 116 (2006) 2-10.

[6] Feng Pan, John Lee, Alex Di Sciullo Jones and Adam Huang, "Improved Micro patterning of Soft-polymers and Elastomers Using Conformally Coated Omni Coat Nanofilms," 2008 ASM International Mechanical Engineering Congress and Exposition, Boston, MA, October 31-November 6, 2008.

[7] V.M. Salinas-Bravo, J. Porcayo-Calderon, and J. G. Gonzalez-Rodriguez., Corrosion Monitoring. Using Electrical Noise and Linear Polarization Resistance in Fuel Oil Combustion Gas Environment. Russian Journal of Electrochemistry, 2006, Vol. 42, No 5, pp 560-565.

[8] Pierre R. Roberge. *Corrosion Inspection and Monitoring* · John Wiley & Sons 2007

[9] G. R. Ruschau, S. Yoshikawa, and R. E. Newnham., Resistivities of Conductive Composites, J. Appl. Phys. 72(3), 1 August 1992.

[10] N. Kchit, G. Bossis, Electrical resistivity mechanism in magnetorheological elastomer. J of Physics D: Applied Physics 42(2009) 105505 (8pp).

[12] Roberge, P.R., (2000) Handbook of Corrosion Engineering. McGraw-Hill, New York

[13] Callister, W. D., (1994) Material Scinece and Engineering, An Introduction. John Wiley&Sons Inc., New York.

[14] Feng Pan, John Lee, Alex Di Sciullo Jones and Adam Huang, "Improved Micro-patterning of Soft-polymers and Elastomers Using Conformally Coated Omni-Coat Nanofilms," 2008 ASME International Mechanical Engineering Congress and Exposition, Boston, MA, October 31-November 6, 2008

[15] Joel Kopinsky, Rutherford Aris, E. L. Cussler Theories of Precipitation Induced by Dissolution. AIChE Jourrnal Vol.34, No.12. December, 1988.

[16] Myles D. Crawford, Jerry Baumgart, Mahnoosh Shoaei, and William R. Ernst. Kinetics of the Dissoution of Alumina in Acidic Solution in a FlowSystem. AIChE Jourrnal Vol.34, No.12. December, 1988.

[17] G. R. Ruschau, S. Yoshikawa, and R. E. Newnham. Percolation Constraints in the Use of Conductor-Filled Polymers for Interconnects. 0569-5503/92/0000-0481 1992 IEEE

[18] R. L. pila and J. D. Sinclair Electrical Reliability of Silver Filled Epoxies for Die Attach. CH2113-9/85/0000-0164 1985 IEEE/IRPS.

[19] Y. Arakawa, Y. Suzuki, N. Kasagi, Micro seismic power generator using electret polymer film, in: Tech. Digest of Power MEMS, Kyoto, Japan, 28– 30 November, 2004–2004, pp. 187–190.

[20] "Omnicoat." MicroChem Corp. 21 June 2007 <http://www.microchem.com/products/pdf/OMNICOAT.pdf>.

[21] J.W.L. Zhou, H.-Y. Chan, T.K.H. To, K.W.C. Lai, W.J. Li, Polymer MEMS actuators for underwater micromanipulation, IEEE/ASME Trans. Mech. 9 (2) (2004) 334–342.

[22] B. Harkness, G. Gardner, J. Alger, M. Cummings, J. Princing, Y. Lee, H. Meynen, M. Gonzalez, B. Vandevelde, M.V. Bulcke, C. Winters, E. Beyne, Photopatternable silicone compositions for electronic packaging applications, in: Adv. Resist Tech. Process. XXI, Proceedings of the SPIE 5376, 2004, pp. 517–524.

[23] Y. Xia, G.M. Whitsides, Soft Lithography, Angew Chem. Int. Edit 37 (1998) 550–575.

[24] W.R. Childs, R.G. Nuzzo, Decal transfer microlithography: a new soft-lithographic patterning method, J. Am. Chem. Soc. 124 (2002) 13583–13596.

[25] K.S. Ryu, K. Shaikh, C. Liu, A method to monolithically integrate elastomer O-rings on parylene membranes for improved valve sealing,in: Proc MicroTAS, 2003, pp. 343–346.

[26] K.S. Ryu, X. Wang, K. Shaikh, C. Liu, A method of precision patterning of silicone elastomer and its applications, J. Microelectromech. Syst. 13 (4) (2004) 568–575.

[27] V.T.S. Wong, A. Huang, C.M. Ho, SU-8 lift-off patterned silicone chemical vapor sensing arrays, in: Proceedings of the 18th IEEE Inernational Conference on Micro-Electro-Mechanical Systems (MEMS2005), Miami Beach, Florida, 30 January to 3 February, 2005, pp. 754–757.

[28] V.T.S. Wong, A. Huang, C.M., Ho, Toward high density silicone polymeric chemical vapor sensor arrays, in: Proceedings of the 11th Inernational Symposium on Olaf. and Electronic Nose (ISOEN), Barcelona, Spain, 13–15 April 2005, pp. 398–401.

[29] B. Matthews, J. Li, S. Sunshine, L. Lerner, J.W. Judy, Effects of electrode configuration on polymer carbon-black composite chemical vapor sensor performance, IEEE Sens. J. 2 (3) (2002) 160–168.

[30] M.C. Lonergan, E.J. Severin, B.J. Doleman, S.A. Beaber, R.H. Grubbs, N.S. Lewis, Array-based vapor sensing using chemically sensitive, carbon black-polymer resistors, Chem. Mater. 8 (9) (1996) 2298–2312.

[31] S.M. Briglin, N.S. Lewis, Characterization of the temporal response profile of carbon black-polymer composite detectors to volatile organic vapors, J. Phys. Chem. B 107 (40) (2003) 11031–11042.

[32] E.J. Severin, B.J. Doleman, N.S. Lewis, An investigation of the concentration dependence and response to analyte mixtures of carbon black/insulating organic polymer composite vapor detectors, Anal. Chem. 72 (4) (2000) 658–668.

[33] "SU-8." MicroChem Corp. 21 June 2007 <http://microchem.com/products/su_eight.htm>.

[34] Russell D. Kane "A New Approach to Corrosion Monitoring" *Chemical Engineering.* June 2007

[35] Milan Kouril, Pavel Novak and Martin Bojko "Limitations of the linear polarization method to determine stainless steel corrosion rate in concrete environment". *Cement & Concrete Composite* 28 (2006) 220-225.

[36] Spomenka Simovic and Clive A. Prestidge "Adsorption of Hydrophobic Silica Nanoparticles at the PDMS Droplet-Water Interface". *Langmuir* 2003 19, 8364-8370.

[37] Charati, S.G. and Stern, S.A. (1998) Diffusion of gases in silicone polymers: Molecular dynamics simulations. Macromolecules, 31, 5529.

[38] Jawalkar, S.S. and Aminabhavi, T.M. (2007) Molecular dynamics simulations to compute diffusion coefficients of gases into polydimethylsiloxane and poly{(1,5-naphthalene)-co- [1,4-durene-2,2 prime -bis(3,4-dicarboxyl phenyl)hexafluoropropane diimide]}. Polymer International, 56, 928.

[39] Pant, K.P.V. and Boyd, R.H. (1993) Molecular dynamics simulation of diffusion of small penetrants in polymers. Macromolecules, 26, 679.

[40] Sok, R.M., Berendsen, H.J.C. and van Gunsteren, W.F. (1992) Molecular dynamics simulation of the transport of small molecules across a polymer membrane. Journal of Chemical Physics, 96, 4699.

[41] Tamai, Y., Tanaka, H. and Nakanishi, K. (1994) Molecular simulation of permeation of small penetrants through membranes. 1. Diffusion coefficients. Macromolecules, 27, 4498.

[42] Burkhart, C.W. (1998) Structurally realistic modeling of elastomers. Rubber Chemistry and Technology, 71, 342.

[43] Frenkel, D. and Smit, B., (2002) *Understanding Molecular Simulation*. Academic Press, San Diego, CA.

[44] Robert Bogue, *MEMS sensors: past, present and future*. Sensor Review 27/1 (2007) 7-13.